

Motion Planning for Variable Topology Trusses: Reconfiguration and Locomotion

Chao Liu¹, Sencheng Yu², and Mark Yim¹

Abstract

Truss robots are highly redundant parallel robotic systems and can be applied in a variety of scenarios. The variable topology truss (VTT) is a class of modular truss robot. As self-reconfigurable modular robots, variable topology trusses are composed of many edge modules that can be rearranged into various structures with respect to different activities and tasks. These robots are able to change their shapes by not only controlling joint positions which is similar to robots with fixed morphologies, but also reconfiguring the connections among modules in order to change their morphologies. Motion planning is the fundamental to apply a VTT robot, including reconfiguration to alter its shape, and non-impact locomotion on the ground. This problem for VTT robots is difficult due to their non-fixed morphologies, high dimensionality, the potential for self-collision, and complex motion constraints. In this paper, a new motion planning framework to dramatically alter the structure of a VTT is presented. It can also be used to solve locomotion tasks much more efficient compared with previous work. Several test scenarios are used to show its effectiveness.

Keywords

Modular Robots, Parallel Robots, Motion Planning, Reconfiguration Planning, Locomotion

1 Introduction

Self-reconfigurable modular robots consist of repeated building blocks (modules) from a small set of types with uniform docking interfaces that allow the transfer of mechanical forces and moments, electrical power, and communication throughout all modules (Yim et al. 2007). These systems are capable of reconfiguring themselves in order to handle failures and adapt to different tasks.

Many self-reconfigurable modular robots have been developed, with the majority being lattice or chain type systems. In lattice modular robots, such as Telecubes (Suh et al. 2002) and Miche (Gilpin et al. 2008), modules are regularly positioned on a three-dimensional grid. Chain modular robots, such as PolyBot (Yim et al. 2000), M-Tran (Murata et al. 2002), and CKBot (Yim et al. 2009), consist of modules that form tree-like structures with kinematic chains that can act like articulated robot arms. Some systems, such as SUPERBOT (Salemi et al. 2006) and SMORES-EP (Liu et al. 2019a) are hybrid and move like chain systems for articulated tasks but reconfigure using lattice-like actions.

Modular truss robots are different from lattice and chain type systems in that the systems are made up of beams that typically form parallel structures. The variable geometry truss (VGT) (Miura 1984) is a modular robotic truss system composed of prismatic joints as truss members (modules), and examples include TETROBOT by Hamlin and Sanderson (1997), Odin by Lyder et al. (2008), and Linear Actuator Robots by Usevitch et al. (2017). These truss members alter their length to perform locomotion or shape-morphing tasks. Another similar hardware is Intelligent Precision Jigging Robots by Komendera and Correll (2015). The **variable topology truss (VTT)** is similar to variable

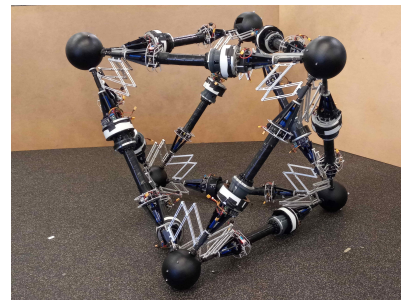


Figure 1. The hardware prototype of a VTT in octahedron configuration is composed of 12 members. Note that at least 18 members are required for topology reconfiguration Spinos et al. (2017).

geometry truss robots with additional capability to self-reconfigure the connection between members to alter the truss topology (Spinos et al. 2017; Jeong et al. 2018). One of the current hardware prototypes is shown in Figure 1.

A significant advantage for self-reconfigurable modular robots over other robots with fixed morphologies is their versatility, namely they are able to adapt themselves into different morphologies with regard to different requirements. For example, a VTT in which the members form a broad supported structure is well-suited for shoring damaged

¹University of Pennsylvania, USA

²Texas A&M University, USA

Corresponding author:

Chao Liu, GRASP Laboratory and The Department of Mechanical Engineering and Applied Mechanics, University of Pennsylvania, 220 South 33rd St., Philadelphia, PA, USA.

Email: chaoliu@seas.upenn.edu

buildings to enable rescue operations. Another truss with some members protruding to form an arm may have a large reachable workspace that is good at manipulation tasks. However, a fundamental complication with VTT systems comes from the motion of the complex parallel structures that may result in self-collision. Developing self-collision-free motion plans is difficult due to the large number of degrees of freedom leading to large search space.

A truss is composed of truss members (beams) and nodes (the connection points of multiple beams). A VTT is composed of *edge modules* each of which is one active prismatic joint member and one passive joint end that can actively attach or detach from other edge module ends (Spinos et al. 2017). The *configuration* can be fully defined by the set of member lengths and their node assignments at which point the edge modules are joined. A node is constructed by multiple edge module ends using a linkage system with a passive rotational degree of freedom. The node assignments define the topology or how truss edge modules are connected, and the length of every member defines the shape of the resulting system (Liu and Yim 2019). Thus, there are two types of reconfiguration motions: *geometry reconfiguration* and *topology reconfiguration*. Geometry reconfiguration involves moving positions of nodes by changing length of corresponding members and topology reconfiguration involves changing the connectivity among members.

There are some physical constraints for a VTT to execute geometry reconfiguration and topology reconfiguration. A VTT has to be a rigid structure in order to maintain its shape and be statically determinant. A node in a VTT must be of degree three, so has to be attached by at least three members to ensure its controllability. In addition, A VTT requires at least 18 members before topology reconfiguration is possible (Spinos et al. 2017). Thus, motion planning for VTT systems has to deal with at least 18 dimensions and typically more than 21 dimensions. These constraints complicate the motion planning problem.

As VTTs are inherently parallel robots, it is much easier to solve the inverse kinematics than the forward kinematics. So, for the geometry reconfiguration, rather than doing motion planning for the active degrees of freedom — the member lengths — we plan the motion of the *nodes* and then do the inverse kinematics to easily determine member lengths. However, the arrangement of edge modules in a VTT can result in a complicated configuration space even for a single node while keeping the others rigid, and motions of multiple nodes are strongly coupled, namely moving one node can significantly affect the configuration space of other nodes.

Some desired node motions are impossible to do without self-collision. These can become possible with topology reconfiguration. For example, a single node controlled by enough edge modules can be split into a pair of nodes in order to go around some internal blocking members and then merge back to an individual node. This process requires motion planning for two nodes at the same time. In addition to shape morphing tasks, this motion planning problem is also the fundamental to solve locomotion tasks for a VTT. Multiple nodes have to move in cooperation in order to move the robot on some terrain while maintaining physical constraints.

Self-reconfiguration enables a VTT to be better suited for a variety of tasks by dramatically changing its shape and topology. Locomotion is one important task in many scenarios. For example, in a search and rescue mission, a VTT may need to flexibly locomote over some terrain to reach a destination and then reconfigure into a tower for shoring. The locomotion process can be achieved by moving nodes sequentially that can interact with the environment. One way to move would be quasi-statically to reduce potentially damaging impacts with the ground (Park et al. 2019).

This paper builds on a sampling-based motion planning framework presented in our previous conference paper (Liu et al. 2020). In this conference paper, we showed that the geometry reconfiguration planning can be solved efficiently by explicitly computing the configuration space for a group of nodes resulting in smaller sampling space and a simpler collision model. We also extended the approach by Liu et al. (2020) to compute all separated enclosed free spaces for a single node so that a sequence of topology reconfiguration actions can be computed by exploring these spaces using a simple rule. This paper adds significantly beyond the conference version in the following. We first extend our configuration space algorithm to take the geometry size of the robot into account. Then more physical hardware constraints are incorporated into the framework. A sampling method is presented to generate enough samples in every enclosed free space that can provide topology reconfiguration actions as many as possible and also cover the space as much as possible. Then these samples can be used to search a sequence of actions for a given reconfiguration task. Finally, we present a novel locomotion framework based on this motion planning approach which provides more robust and efficient performance compared with existing locomotion planning algorithms for truss robots.

The rest of the paper is organized as follows. Section 2 reviews relevant and previous works and some necessary concepts are introduced in Section 3 as well as the problem statement, including reconfiguration and locomotion. Variable topology truss kinematics is introduced in Section 4. Section 5 presents the geometry reconfiguration algorithm with motion of multiple nodes involved considering physical hardware geometry and constraints. Section 6 introduces the approach to verify whether a topology reconfiguration action is needed and the planning algorithm to do topology reconfiguration. The locomotion planning approach is discussed in Section 7. Our framework is demonstrated in several test scenarios in Section 8. Finally, Section 9 talks about the conclusion and some future work.

2 Related Work

In order to enable modular robotic systems to adapt themselves to different activities and tasks, many reconfiguration motion planning algorithms have been developed over several decades for a variety of modular robotic systems (Casal and Yim 1999; Butler et al. 2004; Hou and Shen 2014; Liu et al. 2019a). The planning frameworks are for topology reconfiguration where undocking (disconnecting two attached modules) and docking (connecting

two modules) actions are involved. There are also some approaches for shape morphing and manipulation tasks, including inverse kinematics for highly redundant chain using PolyBot (Agrawal et al. 2001), constrained optimization techniques with nonlinear constraints (Fromherz et al. 2001), and a quadratic programming approach with linear constraints to solve control and motion planning simultaneously in real time (Liu and Yim 2021). In these works, there are no topology reconfiguration actions involved, but complicated kinematic structures and planning in high dimensional spaces need to be considered. However, these methods are not applicable to variable topology truss systems which have a very different morphology and connection architecture. Indeed the physical constraints and collision models are significantly different from all of the previous lattice and chain type systems.

Some approaches have been developed for VGT systems that are similar to VTT systems but without topology reconfiguration capability. Hamlin and Sanderson (1997) presented a kinematic control but is limited to tetrahedrons or octahedrons. Usevitch et al. (2017) introduced linear actuator robots (LARs) as well as a shape morphing algorithm. These systems are in mesh graph topology constructed by multiple convex hulls, and therefore self-collision can be avoided easily. However, this does not apply to VTT systems because edge modules span the space in a very non-uniform manner. There has been some work on VTT motion planning. Retraction-based RRT algorithm was developed by Jeong et al. (2018) in order to handle this high dimensional problem with narrow passage difficulty which is a well-known issue in sampling-based planning approaches; nevertheless, this approach is not efficient because it samples the whole workspace for every node and collision checking needs to be done for every pair of members. Also, sometimes waypoints have to be assigned manually. Liu and Yim (2019) presented a reconfiguration motion planning framework inspired by the DNA replication process — the topology of DNA can be changed by cutting and resealing strands as tanglements form. This work is based on a new method to discretize the workspace depending on the space density and an efficient way to check self-collision. Both topology reconfiguration actions and geometry reconfiguration actions are involved if needed. However, only a single node is involved in each step and the transition model is more complicated, which makes the algorithm limited in efficiency.

Liu et al. (2020) presented a fast algorithm to compute the reachable configuration space of a given node in a VTT which is usually a non-convex space and this space can be then decomposed into multiple convex polyhedrons so that a simple graph search algorithm can be applied to plan a path for this node efficiently. However, multiple nodes are usually involved in shape morphing. In this paper, we first extend this approach to compute the obstacles for multiple nodes so that the search space can be decreased significantly. In addition, only the collision among a small number of edge modules needs to be considered when moving multiple nodes at the same time. Hence sampling-based planners can be applied efficiently. The idea has been discussed briefly by Liu et al. (2019b). For some motion tasks, topology reconfiguration is required. An updated algorithm is developed to compute the whole not fully connected free space and required topology

reconfiguration actions can then be generated which can achieve behaviors that are similar to the DNA replication process.

The VTT locomotion process is similar to a locomotion mode of some VGTs which is accomplished by tipping and contacting the ground. TETROBOT systems and others have been shown with this mode in simulation with generated paths for moving nodes (Woo Ho Lee and Sanderson 2002; Abrahantes et al. 2010). These works divide the locomotion gait into several steps, but they have to compute the motion of nodes beforehand which cannot be applied to arbitrary configurations. Optimization approaches have been used for locomotion planning. Usevitch et al. (2017) formulates the locomotion process as a quadratic program by constraining the motion of the center of mass. The objective function is related to the velocity of each node. A more complete quadratic programming approach to locomotion is presented by Usevitch et al. (2020) to generate discrete motions of nodes in order to follow a given trajectory or compute a complete gait cycle. More hardware constraints were considered, including length and collision avoidance. However, the approach has to solve an optimization problem in high dimensional space, and it also has to deal with non-convex and nonlinear constraints which may cause numerical issues and is limited to a fully connected five-node graph in order to avoid incorporating the manipulability constraints into the quadratic program. Park et al. (2019) extends this optimization-based approach by preventing a robot from receiving impacts from the ground. Incorporated with a polygon-based random tree search algorithm to output a sequence of supporting polygons by Park et al. (2020), a VTT can execute a locomotion task in an environment. However, in these quadratic programs, numerical differentiation is required to relate some physical constraints with these optimized parameters whenever solving the problem. A locomotion step has to be divided into multiple phases leading to more constraints. Also, these approaches are not guaranteed to provide feasible solutions and they are also time-consuming to solve. In this paper, we present a new locomotion planning solution based on our efficient geometry reconfiguration planning algorithm. Our solution can solve the problem much faster and more reliably under several hardware constraints compared with previous works. This approach can be applied to any arbitrary truss robot.

3 Preliminaries and Problem Statement

A VTT can be represented as an undirected graph $G = (V, E)$ where V is the set of vertices of G and E is the set of edges of G : each member can be regarded as an undirected labeled edge $e \in E$ of the graph and every intersection among members can be treated as a vertex $v \in V$ of the graph denoting a node. The Cartesian coordinates of a node $v \in V$ is encoded as its property Pos such that $v[\text{Pos}] = [v_x, v_y, v_z]^T \in \mathbb{R}^3$. Let $q^v = v[\text{Pos}]$ and the *configuration space* of node v denoted as \mathcal{C}^v is simply \mathbb{R}^3 . In this way, the state of a member $e = (v_1, v_2) \in E$ where v_1 and v_2 are two vertices of edge e can be fully defined by q^{v_1} and q^{v_2} . The position of a given node $v \in V$ is controlled by changing the lengths of all attached members denoted as $E^v \subseteq E$.

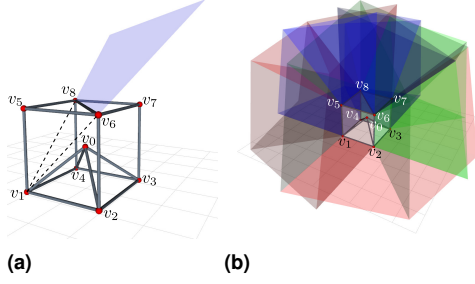


Figure 2. (a) Given node v_0 , one of its neighbors v_1 and a member (v_6, v_8) can define the blue polygon which is part of $C_{\text{obs}}^{v_0}$. (b) The obstacle region $C_{\text{obs}}^{v_0}$ is composed of polygons and the leftover space of \mathbb{R}^3 is $C_{\text{free}}^{v_0}$.

The geometry reconfiguration motion planning of a VTT is achieved by planning the motion of the involved nodes then determining the required member length trajectories since it is easier to solve the inverse kinematics problem. Given a node $v \in V$ in $G = (V, E)$, the state of every member $e \in E^v$, denoted as $\mathcal{A}^v(q^v)$, can be altered by changing q^v . The *obstacle region* of this node which includes self-collision with other members as obstacles $C_{\text{obs}}^v \subseteq C^v = \mathbb{R}^3$ is defined as

$$C_{\text{obs}}^v = \{q^v \in \mathbb{R}^3 | \mathcal{A}^v(q^v) \cap \mathcal{O}^v \neq \emptyset\} \quad (1)$$

in which \mathcal{O}^v is the obstacle for E^v . Liu et al. (2020) proved that this obstacle region is fully defined by the states of $\forall e \in E \setminus E^v$ and composed of multiple polygons. For a simple VTT shown in Figure 2a, the obstacle region $C_{\text{obs}}^{v_0}$ is shown in Figure 2b. The *free space* of node v is just the leftover configurations denoted as

$$C_{\text{free}}^v = \mathbb{R}^3 \setminus C_{\text{obs}}^v \quad (2)$$

However, C_{free}^v may not be fully connected and may be partitioned by C_{obs}^v . Only the enclosed subspace containing q^v which is denoted as $C_{\text{free}}^v(q^v)$ is free for node v to move. A fast algorithm to compute the boundary of this subspace is presented by Liu et al. (2020). For example, given the VTT in Figure 2a, $C_{\text{free}}^{v_0}$ — the free space of v_0 — is partitioned by $C_{\text{obs}}^{v_0}$ in Figure 2b, and the subspace $C_{\text{free}}^{v_0}(q^{v_0})$ is shown in Figure 3.

C_{free}^v is usually partitioned by C_{obs}^v into multiple enclosed subspaces, and it is impossible to move v from one enclosed subspace to another one without topology reconfiguration. The physical system constraints (Spinosa et al. 2017) allow two atomic actions on nodes that enable topology reconfiguration: *Split* and *Merge*. Since the physical system must be statically determinate with all nodes of degree three, a node v must be composed of six or more edge modules to undock and split into two new nodes v' and v'' , and both nodes should still have three or more members. This process is called *Split*. Two separate nodes are able to merge into an individual one in a *Merge* action. The simulation of these two actions is shown in Figure 4. Hence, in a topology reconfiguration process, the number of nodes can change, but the number of members that are physical elements remains constant.

In this work, given a VTT $G = (V, E)$, the reconfiguration planning problem can be stated as the following:

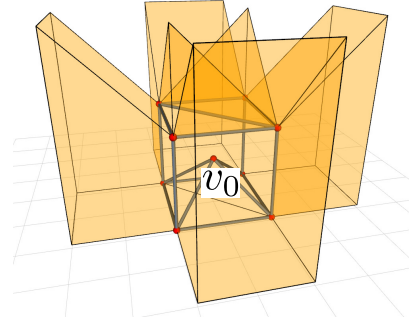


Figure 3. $C_{\text{free}}^{v_0}(q^{v_0})$ is bounded by polygons and workspace boundaries.

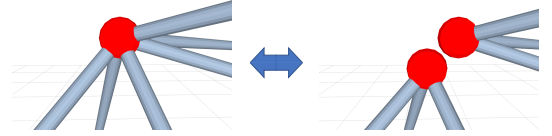


Figure 4. A single node with six members can be split into a pair of nodes and two separate nodes can also merge into an individual node.

- **Geometry Reconfiguration.** For a set of n nodes $\{v_t \in V | t = 1, 2, \dots, n\}$, compute paths $\tau_t : [0, 1] \rightarrow C_{\text{free}}^{v_t}$ such that $\tau_t(0) = q_i^{v_t}$ and $\tau_t(1) = q_g^{v_t}$ in which $t = 1, 2, \dots, n$, $q_i^{v_t}$ is the initial position of v_t and $q_g^{v_t}$ is the goal position of v_t , while satisfying all constraints.
- **Topology Reconfiguration.** Compute the topology reconfiguration actions, *Merge* and *Split*, and find collision-free path(s) to move a node v from its initial position q_i^v to its goal position q_g^v , while satisfying all constraints.

The shape of a VTT $G = (V, E)$ can be regarded as a polyhedron with flat polygonal facets formed by members. This polyhedron consists of vertices (a subset of V), edges, facets F , and an incidence relation on them, e.g. every edge is incident to two vertices and every edge is incident to two facets (Kettner 1999). One of the facets $f \in F$ is the current support polygon. In a rolling locomotion step, the support polygon is changed from f to an adjacent facet f' . As mentioned, impact from the ground can damage the robot, so the stability criterion has to be maintained during the whole process. The locomotion problem for a given VTT $G = (V, E)$ can be stated in the following:

- **Non-impact Rolling Locomotion.** Compute the motion of a set of nodes in V to change the support polygon from $f \in F$ to a desired adjacent facet $f' \in F$ without receiving impacts from the ground while satisfying all constraints.

4 Robot Kinematics and Hardware Constraints

Given a VTT $G = (V, E)$, motion of nodes are controlled by all attached actuated members and the system is usually an overconstrained parallel robot. The set of all nodes V is separated into two groups: V_F and V_C where V_F contains

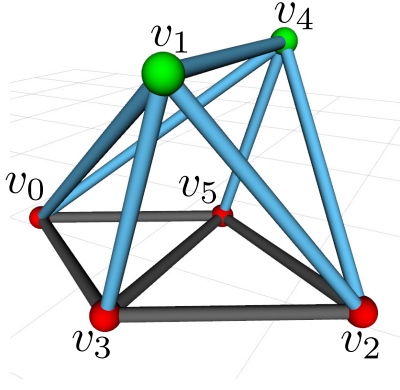


Figure 5. A VTT is composed of twelve members. Currently, the motion of node v_1 and node v_4 are under control by seven blue members.

all the fixed or stationary nodes and V_C contains all the controlled nodes. For example, given the VTT shown in Figure 5, when controlling the motion of node v_1 and node v_4 , $V_C = \{v_1, v_4\}$ and $V_F = \{v_0, v_2, v_3, v_5\}$, and this is a 6-DOF system since there are two controlled nodes. In addition, this system is overconstrained and the motion of two nodes are controlled by seven members. Note that V_F and V_C are not constant and they can be changed during the motion of a VTT (reconfiguration and locomotion).

4.1 Robot Kinematics

Given V_C with Λ nodes under control, the position vector of this system is simply the stack of q^v where $v \in V_C$, and this system is controlled by all members that are attached with these nodes, namely $\bigcup_{v \in V_C} E^v$. Let l_{ij} be the link vector from a controlled node v_i pointing to any node v_j . There are two types of link vectors: 1. if $v_j \in V_F$, then l_{ij} is an attachment link vector; 2. if $v_j \in V_C$, then l_{ij} is a connection link vector. The link vector satisfies the following equation:

$$l_{ij} = q^{v_j} - q^{v_i} \quad (3)$$

in which $v_i \in V_C$. Taking time derivative of Eq. (3) for an attachment link vector and a connection link vector yields

$$l_{ij}^T \dot{l}_{ij} = (q^{v_i} - q^{v_j})^T \dot{q}^{v_i} \quad \forall v_j \in V_F \quad (4a)$$

$$\dot{l}_{ij} = \dot{q}^{v_j} - \dot{q}^{v_i} \quad \forall v_j \in V_C \quad (4b)$$

Assume $V_C = \{\bar{v}_\alpha | \alpha = 1, 2, \dots, \Lambda\}$, and for a controlled node \bar{v}_α , all the fixed nodes in its neighborhood $\mathcal{N}_G(\bar{v}_\alpha)$ are denoted as $\hat{v}_1^\alpha, \hat{v}_2^\alpha, \dots, \hat{v}_N^\alpha$, and the corresponding attachment link vectors are denoted as ${}^\alpha \hat{l}_1, {}^\alpha \hat{l}_2, \dots, {}^\alpha \hat{l}_N$. Eq. (4a) is true for any ${}^\alpha \hat{l}_t$ where $t \in [1, N]$, so we can rewrite it into the following form for a controlled vertex v_i

$$B_\alpha \dot{L}_\alpha = A_\alpha \dot{q}^{\bar{v}_\alpha} \quad (5)$$

in which

$$\dot{L}_\alpha = \begin{bmatrix} {}^\alpha \dot{\hat{l}}_1^T & {}^\alpha \dot{\hat{l}}_2^T & \dots & {}^\alpha \dot{\hat{l}}_N^T \end{bmatrix}_{3N \times 1}^T$$

$$B_\alpha = \begin{bmatrix} {}^\alpha \hat{l}_1^T & 0 & \dots & 0 \\ 0 & {}^\alpha \hat{l}_2^T & \dots & 0 \\ \vdots & \vdots & \ddots & \vdots \\ 0 & 0 & \dots & {}^\alpha \hat{l}_N^T \end{bmatrix}_{N \times 3N}$$

$$A_\alpha = \begin{bmatrix} q^{\bar{v}_\alpha} - q^{\hat{v}_1^\alpha} & q^{\bar{v}_\alpha} - q^{\hat{v}_2^\alpha} & \dots & q^{\bar{v}_\alpha} - q^{\hat{v}_N^\alpha} \end{bmatrix}_{N \times 3}^T$$

If another controlled node $\bar{v}_\beta \in \mathcal{N}_G(\bar{v}_\alpha)$, namely \bar{v}_β is adjacent to \bar{v}_α , then we have

$$\dot{l}_{\alpha\beta} = \dot{q}^{\bar{v}_\beta} - \dot{q}^{\bar{v}_\alpha} \quad (6)$$

Combining Eq. (5) and Eq. (6), the following equation of motion can be derived

$$\mathcal{B} \dot{\mathcal{L}} = \mathcal{A} \dot{p} \quad (7)$$

in which

$$p = \begin{bmatrix} (q^{\bar{v}_1})^T & (q^{\bar{v}_2})^T & \dots & (q^{\bar{v}_\Lambda})^T \end{bmatrix}^T$$

$$\dot{\mathcal{L}} = \begin{bmatrix} \dot{L}_1^T & \dot{L}_2^T & \dots & \dot{L}_\Lambda^T & \dots & \dot{l}_{\alpha\beta} & \dots \end{bmatrix}^T$$

$$\mathcal{B} = \text{diag}(B_1, B_2, \dots, B_\Lambda, \dots, I, \dots) \quad \mathcal{A} = [A_1, A_2]^T$$

$$A_1 = \text{diag}(A_1, A_2, \dots, A_\alpha, \dots, A_\beta, \dots, A_\Lambda)$$

$$A_2 = \begin{bmatrix} \vdots & \vdots & \vdots & \vdots & \vdots \\ 0_{3 \times 3\alpha} & I_{3 \times 3} & 0_{3 \times (\beta - \alpha - 1)} & -I_{3 \times 3} & 0_{3 \times 3(\Lambda - \beta)} \\ \vdots & \vdots & \vdots & \vdots & \vdots \end{bmatrix}$$

The size of \mathcal{A}_2 is determined by the number of controlled vertices and connection link vectors (if there are ω connection link vectors, \mathcal{A}_2 is a $3\omega \times 3\Lambda$ matrix). For the system shown in Figure 5, $\mathcal{A}_2 = [I, -I]_{3 \times 6}$ since there are only two controlled nodes and one connection link vector. It can be shown that \mathcal{B} has full rank as long as there are no zero-length members whereas \mathcal{A} may not have full rank. This does make sense because there must exist a set of link velocities given the velocities of all controlled nodes, but some link velocities may result in invalid motions of nodes since the system can be overconstraint.

We can rearrange Eq. (7) in two ways:

$$\dot{\mathcal{L}} = \mathcal{B}^+ \mathcal{A} \dot{p} = J_{BA} \dot{p} \quad (8a)$$

$$\dot{p} = \mathcal{A}^+ \mathcal{B} \dot{\mathcal{L}} = J_{AB} \dot{\mathcal{L}} \quad (8b)$$

where \mathcal{B}^+ and \mathcal{A}^+ are the pseudo-inverse of \mathcal{B} and \mathcal{A} respectively, and both J_{BA} and J_{AB} matrices are the Jacobian. We use these two equations to describe the relationship between the link velocities and the controlled node velocities. J_{BA} is always defined (as long as there is no zero-length member), but J_{AB} may not be defined. Given \dot{p} is known, Eq. (8a) gives the minimum norm solution to Eq. (7), namely minimizing $\|\dot{\mathcal{L}}\|$. On the other hand, Eq. (8b) results in the unique least square solution to Eq. (7) if $\dot{\mathcal{L}}$ is known, namely minimizing $\|\mathcal{B} \dot{\mathcal{L}} - \mathcal{A} \dot{p}\|$.

4.2 Hardware and Environmental Constraints

A VTT has to maintain some hardware constraints during its motion, and this includes the limitations from the hardware, the stability and controllability of the system, and impact avoidance in reconfiguration and locomotion activities.

4.2.1 Length Constraints In a VTT, each edge module has an active prismatic joint called Spiral Zipper (Collins and Yim 2016) and this joint is able to achieve a high extension ratio as well as form a high strength to weight ratio column. The mechanical components determine the minimum member length and the total material determines the maximum member length. Hence, in a VTT $G = (V, E)$, $\forall e = (v_i, v_j) \in E$, we have the following constraint

$$\bar{L}_{\min}^2 \leq \|q^{v_i} - q^{v_j}\| \leq \bar{L}_{\max}^2 \quad (9)$$

4.2.2 Collision Avoidance During the motion of a VTT, we have to avoid the collision between members. The distance between every two members have to be greater than \bar{d}_{\min} , the diameter of an edge module which is a cylinder (or the sum of the radius of a node and the radius of an edge module). The minimum distance between member (v_i, v_j) and (v_m, v_n) can be expressed as

$$\min \|(q^{v_i} + \alpha(q^{v_j} - q^{v_i})) - (q^{v_m} + \gamma(q^{v_n} - q^{v_m}))\| \quad (10)$$

in which $\alpha, \gamma \in (0, 1)$. This is not easy to compute and can be more complicated when both members are actuating. In Section 5, we will show that our approach doesn't need to solve this problem. We also need to ensure the angle between connected members remains above a certain value due to the mechanical design of the node. The angle constraint between member (v_i, v_j) and (v_i, v_k) can be expressed as

$$\arccos \left(\frac{(q^{v_j} - q^{v_i}) \bullet (q^{v_k} - q^{v_i})}{\|q^{v_j} - q^{v_i}\| \|q^{v_k} - q^{v_i}\|} \right) \geq \bar{\theta}_{\min} \quad (11)$$

4.2.3 Stability The truss structure of a VTT is meant to be statically stable under gravity when interacting with the environment and sufficient constraints between the robot and the environment must be satisfied to ensure the location of the structure is fully defined. At least three still nodes should be on the ground in order to form a valid support polygon. For the VTT shown in Figure 5, v_0, v_2, v_3 , and v_5 are stationary on the ground to form the current support polygon. In addition, the center of mass of a VTT as represented on the ground has to be inside this support polygon. Furthermore, no collision is allowed between a VTT and the environment, and the simplest condition is that all nodes have to be above the ground.

4.2.4 Manipulability In order to control the motion of nodes, a VTT has to maintain an amount of manipulability for these moving nodes. Given a VTT $G = (V, E)$ and the current controlled node set V_C , the Jacobian J_{AB} can be derived as shown in Eq. (8b). By applying singular value decomposition on J_{AB} , its maximum singular value $\sigma_{\max}(J_{AB})$ and minimum singular value $\sigma_{\min}(J_{AB})$ can be derived, and the manipulability of current moving nodes can be constrained as

$$\mu = \frac{\sigma_{\min}(J_{AB})}{\sigma_{\max}(J_{AB})} \geq \bar{\mu}_{\min} \quad (12)$$

5 Geometry Reconfiguration

The overall shape of a VTT is altered by moving nodes around in the workspace. For an individual node, its

configuration space is \mathbb{R}^3 . Apparently, the configuration space for n nodes is \mathbb{R}^{3n} . When multiple nodes are involved, the motion planning problem will be in high-dimensional space. Our strategy to avoid this high dimensionality is to divide the moving nodes into multiple groups and each group contains one or a pair of nodes. The motion planning space for each group is either in \mathbb{R}^3 or \mathbb{R}^6 . Even with lower-dimensional space, it is still a challenge to search for a valid solution. First, it is not efficient to search the whole \mathbb{R}^3 or \mathbb{R}^6 and narrow passage is a significant problem when applying rapidly-exploring random tree (RRT) algorithm. In addition, it is difficult to guarantee the collision avoidance for a given motion by simply discretizing the motion to some resolution and checking states at that resolution because the case that a member goes across another member may not be detected, or very fine resolution has to be used which will slow down the planner significantly. We overcome these issues by computing the free space of the group in advance so that the sampling space is decreased significantly.

5.1 Obstacle Region and Free Space

A group can contain either one node or a pair of nodes. Given a VTT $G = (V, E)$, for an individual node $v \in V$, an efficient algorithm to compute $\mathcal{C}_{\text{obs}}^v$ and $\mathcal{C}_{\text{free}}^v(q^v)$ with its boundary is introduced by Liu et al. (2020). If there are two nodes $v_i \in V$ and $v_j \in V$ in a group, then any collision among members in E^{v_i} and E^{v_j} is treated as self-collision inside the group, and all the members in $E \setminus (E^{v_i} \cup E^{v_j})$ define the obstacle region of this group denoted as $\hat{\mathcal{C}}_{\text{obs}}^{v_i}$ (the obstacle region of v_i in the group) and $\hat{\mathcal{C}}_{\text{obs}}^{v_j}$ (the obstacle region of v_j in the group) respectively, namely

$$\hat{\mathcal{C}}_{\text{obs}}^{v_i} = \{q^{v_i} \in \mathbb{R}^3 | \mathcal{A}^{v_i}(q^{v_i}) \cap \mathcal{O}^{v_i, v_j} \neq \emptyset\}$$

$$\hat{\mathcal{C}}_{\text{obs}}^{v_j} = \{q^{v_j} \in \mathbb{R}^3 | \mathcal{A}^{v_j}(q^{v_j}) \cap \mathcal{O}^{v_i, v_j} \neq \emptyset\}$$

in which \mathcal{O}^{v_i, v_j} is formed by every $e \in E \setminus (E^{v_i} \cup E^{v_j})$.

Then the free space of v_i and v_j in the group can be derived as

$$\hat{\mathcal{C}}_{\text{free}}^{v_i} = \mathbb{R}^3 \setminus \hat{\mathcal{C}}_{\text{obs}}^{v_i} \quad (13)$$

$$\hat{\mathcal{C}}_{\text{free}}^{v_j} = \mathbb{R}^3 \setminus \hat{\mathcal{C}}_{\text{obs}}^{v_j} \quad (14)$$

Using the same boundary search approach in Liu et al. (2020), the boundary of $\hat{\mathcal{C}}_{\text{free}}^{v_i}(q^{v_i})$ — the enclosed subspace containing the current position of node v_i — can be obtained efficiently. Similarly, the boundary of $\hat{\mathcal{C}}_{\text{free}}^{v_j}(q^{v_j})$ can be obtained. For example, given the VTT shown in Figure 6, if node v_0 and v_1 form a group, then $\hat{\mathcal{C}}_{\text{free}}^{v_0}(q^{v_0})$ and $\hat{\mathcal{C}}_{\text{free}}^{v_1}(q^{v_1})$

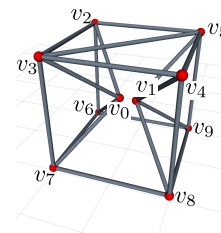


Figure 6. A VTT is composed of 21 edge modules with 10 nodes among which v_0 and v_1 form a group.

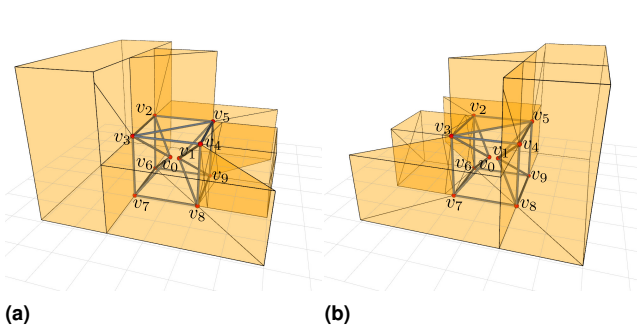


Figure 7. (a) $\hat{C}_{\text{free}}^{v_0}(q^{v_0})$ is computed with all members controlling v_1 ignored. (b) $\hat{C}_{\text{free}}^{v_1}(q^{v_1})$ is computed with all members controlling v_0 ignored.

can be computed and shown in Figure 7. $\hat{C}_{\text{free}}^{v_0}(q^{v_0})$ contains some space on the right side of v_1 because E^{v_1} is ignored. This space informs that it is possible to move v_0 to some locations which are currently blocked by v_1 since v_1 can be moved away. It is guaranteed that as long as v_0 is moving inside $\hat{C}_{\text{free}}^{v_0}(q^{v_0})$ (the space shown in Figure 7a), there must be no collision between any member in E^{v_0} and any member in $E \setminus (E^{v_0} \cup E^{v_1})$. Similarly, no collision between any member in E^{v_1} and any member in $E \setminus (E^{v_0} \cup E^{v_1})$ can happen if v_1 is moving inside $\hat{C}_{\text{free}}^{v_1}(q^{v_1})$ (the space shown in Figure 7b). In this way, when planning the motion of node v_0 and v_1 using RRT, the sample will only be generated inside $\hat{C}_{\text{free}}^{v_0}(q^{v_0})$ and $\hat{C}_{\text{free}}^{v_1}(q^{v_1})$, and we only need to consider self-collision in the group, namely the collision among members in $E^{v_0} \cup E^{v_1}$. There is a special case when these two nodes in the group are connected by a member. Both ends of the member are moving which is not considered by our obstacle model. This is an extra case when doing collision check.

The previous free space and the obstacle region are derived by ignoring the physical size of members and nodes, such as the obstacle polygon shown in Figure 2a that is derived by regarding node v_1 as a point and member (v_6, v_8) as a line segment without thickness. In practice, a node is a sphere and a member is a cylinder, so it is not guaranteed that the minimum distance among members (Eq. 10) is greater than the diameter of an edge module (or the sum of the radius of a node and the radius of an edge module) even the involved node is not inside its obstacle region. This difficulty is overcome through increasing the derived obstacle region by considering the physical size of VTT components. In the obstacle region, every polygon is converted into a polyhedron. For example, for the VTT shown in Figure 2a, the blue polygon defined by node v_1 and edge module (v_6, v_8) is one obstacle polygon for node v_0 , and this polygon is converted into a polyhedron shown in Figure 8. The boundary of this obstacle polyhedron is composed of five polygons that can be obtained as follows:

The current locations of nodes v_1 , v_6 , and v_8 are q^{v_1} , q^{v_6} , and q^{v_8} respectively, and the unit vector normal to the plane formed by these three nodes is \hat{n}_p ($-\hat{n}_p$ is also a normal unit vector but in opposite direction). As shown in Figure 9b, we first adjust q^{v_6} and q^{v_8} by moving them along \hat{n}_p and $-\hat{n}_p$

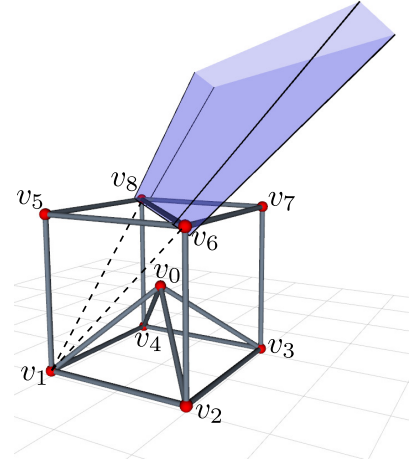


Figure 8. One obstacle polygon of $\mathcal{C}_{\text{obs}}^{v_0}$ shown in Figure 2a becomes a polyhedron bounded by five polygons if the size of VTT components is considered.

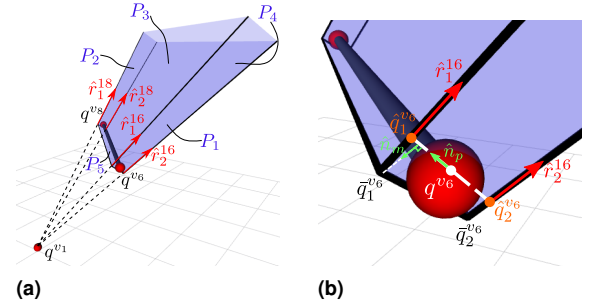


Figure 9. (a) Detailed illustration of the formation of the obstacle polyhedron. (b) Close view of the obstacle polyhedron.

respectively

$$\begin{aligned} \hat{q}_1^{v_6} &= q^{v_6} + \lambda \hat{n}_p, \quad \hat{q}_2^{v_6} = q^{v_6} - \lambda \hat{n}_p \\ \hat{q}_1^{v_8} &= q^{v_8} + \lambda \hat{n}_p, \quad \hat{q}_2^{v_8} = q^{v_8} - \lambda \hat{n}_p \end{aligned}$$

where λ is the growing size, which is taken to be the sum of the radius of the node and the radius of the edge. Then, the four rays shown in Figure 9a can be easily derived

$$\begin{aligned} \hat{r}_1^{16} &= \frac{\hat{q}_1^{v_6} - q^{v_1}}{\|\hat{q}_1^{v_6} - q^{v_1}\|}, \quad \hat{r}_2^{16} = \frac{\hat{q}_2^{v_6} - q^{v_1}}{\|\hat{q}_2^{v_6} - q^{v_1}\|} \\ \hat{r}_1^{18} &= \frac{\hat{q}_1^{v_8} - q^{v_1}}{\|\hat{q}_1^{v_8} - q^{v_1}\|}, \quad \hat{r}_2^{18} = \frac{\hat{q}_2^{v_8} - q^{v_1}}{\|\hat{q}_2^{v_8} - q^{v_1}\|} \end{aligned}$$

\hat{n}_m is the unit vector perpendicular to the edge (v_6, v_8) , pointing to v_1 and lying on the plane formed by v_1 , v_6 , and v_8 . Then $\hat{q}_1^{v_6}$, $\hat{q}_2^{v_6}$, $\hat{q}_1^{v_8}$, and $\hat{q}_2^{v_8}$ are moved by distance $\frac{\lambda}{2}$ on \hat{n}_m along $-\hat{r}_1^{16}$, $-\hat{r}_2^{16}$, $-\hat{r}_1^{18}$, and $-\hat{r}_2^{18}$, respectively:

$$\begin{aligned} \bar{q}_1^{v_6} &= \hat{q}_1^{v_6} - \frac{\lambda}{2|\hat{n}_m \cdot \hat{r}_1^{16}|} \hat{r}_1^{16} \\ \bar{q}_2^{v_6} &= \hat{q}_2^{v_6} - \frac{\lambda}{2|\hat{n}_m \cdot \hat{r}_2^{16}|} \hat{r}_2^{16} \\ \bar{q}_1^{v_8} &= \hat{q}_1^{v_8} - \frac{\lambda}{2|\hat{n}_m \cdot \hat{r}_1^{18}|} \hat{r}_1^{18} \\ \bar{q}_2^{v_8} &= \hat{q}_2^{v_8} - \frac{\lambda}{2|\hat{n}_m \cdot \hat{r}_2^{18}|} \hat{r}_2^{18} \end{aligned}$$

With all the information, we can encode the boundary of the polyhedron that is composed of five polygons shown in Figure 9a in the following

$$\begin{aligned} P_1 &= \{V = (\bar{q}_1^{v_6}, \bar{q}_2^{v_6}), R = (\hat{r}_1^{16}, \hat{r}_2^{16})\} \\ P_2 &= \{V = (\bar{q}_1^{v_8}, \bar{q}_2^{v_8}), R = (\hat{r}_1^{18}, \hat{r}_2^{18})\} \\ P_3 &= \{V = (\bar{q}_1^{v_6}, \bar{q}_1^{v_8}), R = (\hat{r}_1^{16}, \hat{r}_1^{18})\} \\ P_4 &= \{V = (\bar{q}_2^{v_6}, \bar{q}_2^{v_8}), R = (\hat{r}_2^{16}, \hat{r}_2^{18})\} \\ P_5 &= \{V = (\bar{q}_1^{v_6}, \bar{q}_2^{v_6}, \bar{q}_1^{v_8}, \bar{q}_2^{v_8})\} \end{aligned}$$

Note that P_5 consists of no rays.

We can convert every obstacle polygon in Figure 2b into an obstacle polyhedron (bounded by five polygons) in this way, and then process these polygons by *Polygon Intersection and Boundary Search* (Liu et al. 2020) to derive $C_{\text{free}}^{v_0}(q^{v_0})$ shown in Figure 10. The *Boundary Search* step can be simplified and the modified boundary search algorithm is shown in Algorithm 1. Recall that the free space of a node is usually partitioned by its obstacle region into multiple enclosed subspaces, and given an obstacle polygon P_s and the set of all obstacle polygons \mathcal{P}_{obs} generated by *Polygon Intersection* step, this algorithm can find the enclosed subspace with P_s being part of the boundary. Details of *Polygon Intersection* is introduced by Liu et al. (2020), and note that after *Polygon Intersection*, each polygon in \mathcal{P}_{obs} can only bound one enclosed subspace because every obstacle polygon is the boundary between the free space and the obstacle region. If we want to find the boundary of $C_{\text{free}}^{v_0}(q^{v_0})$, we can set P_s to be the obstacle polygon that is closest to q^{v_0} . In the algorithm, S_i is the set of all edges of polygon P_i , s_{ij} is the j th edge of P_i , and \mathcal{N}_{ij} is the set of all polygons that share s_{ij} with P_i . For each obstacle polygon P_i , its normal vector pointing outwards the obstacle region is computed, and \bar{P}_{ij} in Line 8 is the innermost polygon in \mathcal{N}_{ij} along the normal vector of P_i .

The new $C_{\text{free}}^{v_0}(q^{v_0})$ is smaller and bounded by more polygons. In addition to considering the physical size of the robot components, for a single node, we can easily find the region when it is in a singular configuration. For a single node, if all of its neighbor nodes are on the same plane, then

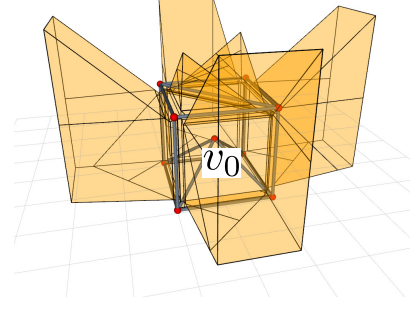


Figure 10. $C_{\text{free}}^{v_0}(q^{v_0})$ with physical size of components being considered.

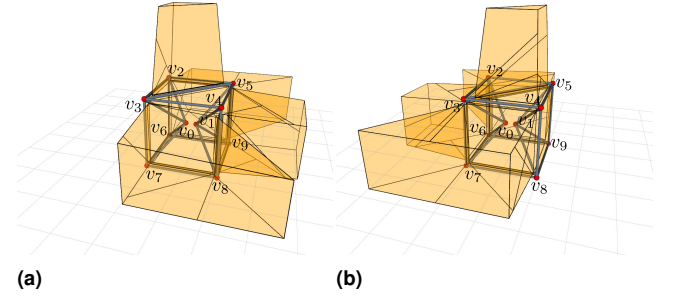


Figure 11. (a) $\hat{C}_{\text{free}}^{v_0}(q^{v_0})$ is computed with all members controlling v_1 ignored. (b) $\hat{C}_{\text{free}}^{v_1}(q^{v_1})$ is computed with all members controlling v_0 ignored.

this node cannot traverse this plane, or it will be in a singular configuration. In such a case, we also add this plane to the obstacle polygon set when running the boundary search algorithm. By taking these constraints into consideration, we can derive $\hat{C}_{\text{free}}^{v_0}(q^{v_0})$ and $\hat{C}_{\text{free}}^{v_1}(q^{v_1})$ for the group containing v_0 and v_1 in the VTT shown in Figure 6 and the result is shown in Figure 11. Compared with the space shown in Figure 7, $C_{\text{free}}^{v_0}(q^{v_0})$ becomes smaller and v_0 cannot go beyond the plane formed by v_2, v_3, v_6 , and v_7 due to the singularity constraint. In the rest of the paper, we will use the free space ignoring the physical sizes of robot components for illustration purposes.

Algorithm 1: Boundary Search Algorithm

Input: $P_s, \mathcal{P}_{\text{obs}}$
Output: A set of boundary polygons \mathcal{P}_b

```

1  $\mathcal{P}_b \leftarrow \emptyset$ ;
2  $\mathcal{Q}_P \leftarrow \emptyset$ ;
3  $\mathcal{Q}_P.\text{enqueue}(P_s)$ ;
4 while  $\mathcal{Q}_P \neq \emptyset$  do
5    $P_i \leftarrow \mathcal{Q}_P.\text{dequeue}()$ ;
6    $\mathcal{P}_b \leftarrow \mathcal{P}_b \cup \{P_i\}$ ;
7   for  $s_{ij} \in S_i$  do
8      $\bar{P}_{ij} \leftarrow$  the innermost polygon in  $\mathcal{N}_{ij}$ ;
9     if  $\bar{P}_{ij} \notin \mathcal{P}_b \wedge \bar{P}_{ij} \notin \mathcal{Q}_P$  then
10        $\mathcal{Q}_P.\text{enqueue}(\bar{P}_{ij})$ ;
11   end
12 end
13 end
14 return  $\mathcal{P}_b$ 

```

5.2 Path Planning for a Group of Nodes

If there is only one node v in the group and the motion task is to move the node from its initial position q_i^v to its goal position q_g^v where $q_i^v \in C_{\text{free}}^v(q_i^v)$ and $q_g^v \in C_{\text{free}}^v(q_i^v)$, then it is straightforward to apply RRT approach in $C_{\text{free}}^v(q_i^v)$ and no collision can happen as long as the motion of each step is inside $C_{\text{free}}^v(q_i^v)$ since this space is usually not convex.

When moving two nodes v_i and v_j in a group, sampling will only happen inside $\hat{C}_{\text{free}}^{v_i}(q^{v_i})$ and $\hat{C}_{\text{free}}^{v_j}(q^{v_j})$ for v_i and v_j respectively. If there is no edge module connecting v_i and v_j , then when applying RRT approach, the collision between moving members and fixed members can be ignored as long as the motion of both nodes in each step are inside $\hat{C}_{\text{free}}^{v_i}(q^{v_i})$ and $\hat{C}_{\text{free}}^{v_j}(q^{v_j})$ respectively. Only self-collision inside the group — the collision among members in $E^{v_i} \cup E^{v_j}$ — needs to be considered. If there is an edge module $e = (v_i, v_j)$ which connects v_i and v_j , since this case is not

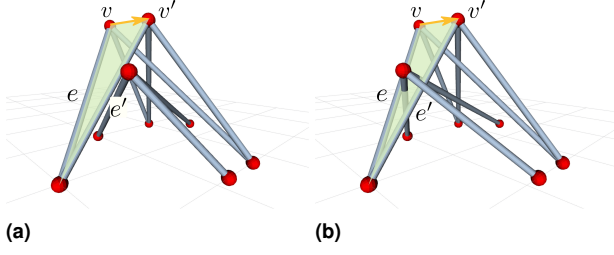


Figure 12. Light green triangle (\triangle) is swept by member e when moving node v to new location v' along the yellow (\rightarrow) trajectory and the new position of member e is e' . e doesn't collide with any other members in (a) but does collide with two members in (b) during the motion (Liu and Yim 2019).

included in our obstacle model when computing the obstacle region for the group, it is also necessary to check the collision between $e = (v_i, v_j)$ and every edge module in $E \setminus (E^{v_i} \cup E^{v_j})$.

In summary, when planning node v_i and v_j in a VTT $G = (V, E)$, for each step, in order to avoid collision, it is required to ensure the following

- The motion of both node v_i and v_j are inside $\hat{C}_{\text{free}}^{v_i}(q^{v_i})$ and $\hat{C}_{\text{free}}^{v_j}(q^{v_j})$ respectively;
- No collision happens among edge modules in $E^{v_i} \cup E^{v_j}$;
- No collision happens between edge module $e = (v_i, v_j)$ and every member in $E \setminus (E^{v_i} \cup E^{v_j})$ if $e = (v_i, v_j)$ exists.

It is difficult to check the second and third collision cases during the motion if both nodes are moving simultaneously. But since the step size for each node is limited and both of them are moving in straight lines, we can first check the collision during the motion of v_i while keeping v_j fixed, and then check the motion of v_j . By doing so, the collision can be checked efficiently using the approach presented by Liu and Yim (2019). Every edge module can be modeled as a line segment in space, thus, when moving node v , every $e \in E^v$ sweeps a triangle area, and if this member collides with another member $\bar{e} \in E$, then \bar{e} must intersect with the triangle generated by e (Figure 12). Similar to the approach in Section 5.1, we can buffer this triangle area in order to consider the size of physical components. Another way is to compute the local obstacle region of v_i by only taking E^{v_j} into account when moving v_i , and similarly compute the local obstacle region of v_j by only taking E^{v_i} into account when moving v_j . The local obstacle region of each node can be derived easily. For v_i , given $\mathcal{N}_G(v_i)$ that is the neighbors of v_i and E^{v_j} , the local obstacle region of v_i is simply the union of all the obstacle polyhedron defined by all $(v, e) \in \mathcal{N}_G(v_i) \times E^{v_j}$. If the trajectory of v_i that is a line segment intersects with its local obstacle region, then collision happens. Repeat the same procedures when moving v_j . If edge module (v_i, v_j) exists, when moving v_i , we also need to consider the obstacle polyhedron defined by v_j and $e \in E \setminus (E^{v_i} \cup E^{v_j})$, and similarly consider the obstacle polyhedron defined by v_i and $e \in E \setminus (E^{v_i} \cup E^{v_j})$ when moving v_j .

In addition to this constraint that the distance between every pair of members has to be greater than some value,

a discrete motion also needs to satisfy the length constraint (Eq. 9), the angle constraint (Eq. 11), the manipulability constraint (Eq. 12), and the stability constraint when interacting with the environment. For these constraints, it is straightforward to discretize the motion in the current step to some resolution and check the states for validity at this resolution. When checking the stability constraint, we first find all supporting nodes by checking the height of every node, and if its height is close enough to the ground, then this node is regarded as a supporting node. There have to be at least three supporting nodes all the time. Otherwise, this VTT cannot be stable. Then the center of mass of the current truss is computed and projected onto the ground. Given this projected center of mass and all supporting nodes on the ground, the convex hull of them (the smallest convex polygon that contains all these points) can be computed efficiently using either Jarvis's march (Jarvis 1973) or Graham's scan (Graham 1972). If the projected center of mass is not on the boundary of the convex hull, then it is inside the support polygon that is the convex hull. Otherwise, this VTT cannot be stable.

With all these works, we can efficiently check the state validity and motion validity, and RRT-type approaches can be applied easily. Open Motion Planning Library (OMPL) by Sucan et al. (2012) is used to implement RRT for this path planning problem.

5.3 Geometry Reconfiguration Planning

Assuming there are n nodes $\{v_t \in V | t = 1, 2, \dots, n\}$ that should be moved from their initial positions $q_i^{v_1}, q_i^{v_2}, \dots, q_i^{v_n}$ to their goal positions $q_g^{v_1}, q_g^{v_2}, \dots, q_g^{v_n}$ respectively, we first divide these nodes into $\lceil n/2 \rceil$ groups. Each group contains at most two nodes. Then the motion task is achieved by moving nodes one group by one group. Then this geometry reconfiguration problem results in finding a sequence of groups that can achieve the task. If failed, try another grouping and find the corresponding sequence. Repeat this process until the task is finished, otherwise failed. With this approach, we can solve this geometry reconfiguration planning problem much faster than the approach by Liu et al. (2020) and the detailed test results are in Section 8.

6 Topology Reconfiguration

Topology reconfiguration involves changing the connectivity among edge modules and there are two atomic actions: Split and Merge. The undocking and docking process is difficult for modular robotic systems, but sometimes necessary for some motion tasks. We need to verify whether the geometry reconfiguration process is enough or topology reconfiguration actions are needed. Recall that the free space of a node is usually not a single connected component and if a motion task has initial and goal configurations in separated enclosed subspaces, topology reconfiguration actions are needed.

6.1 Enclosed Subspace in Free Space

As mentioned before, each polygon after *Polygon Intersection* in $\mathcal{C}_{\text{obs}}^v$ is bounding only one enclosed subspace.

Algorithm 2: Enclosed Subspace Search**Input:** VTT $G = (V, E)$, node $v \in V$ **Output:** Set of all enclosed subspaces $\mathcal{C}_{\text{free}}^v$

```

1 Compute  $\mathcal{P}_{\text{obs}}$ ;
2  $P_s \leftarrow$  polygon closest to node  $v$ ;
3  $\mathcal{C}_{\text{free}}^v(q^v) \leftarrow \text{BoundarySearch}(P_s, \mathcal{P}_{\text{obs}})$ ;
4  $\mathcal{C}_{\text{free}}^v \leftarrow \{\mathcal{C}_{\text{free}}^v(q^v)\}$ ;
5 for  $P_i \in \mathcal{P}_{\text{obs}}$  do
6   if  $P_i \notin \mathcal{C}$ ,  $\forall C \in \mathcal{C}_{\text{free}}^v$  then
7      $\mathcal{C}_{\text{new}} \leftarrow \text{BoundarySearch}(P_i, \mathcal{P}_{\text{obs}})$ ;
8      $\mathcal{C}_{\text{free}}^v \leftarrow \mathcal{C}_{\text{free}}^v \cup \{\mathcal{C}_{\text{new}}\}$ ;
9   end
10 end
11 return  $\mathcal{C}_{\text{free}}^v$ 

```

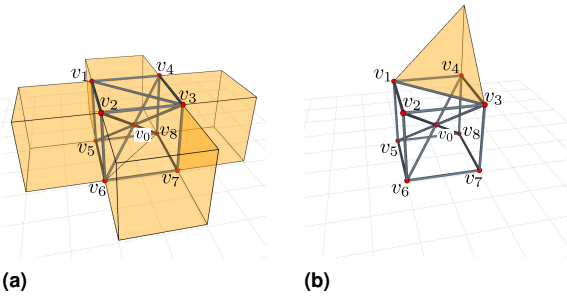


Figure 13. (a) Enclosed subspace $\mathcal{C}_{\text{free}}^{v_0}(q^{v_0})$ contains the current position of v_0 . (b) Another enclosed subspace is separated from $\mathcal{C}_{\text{free}}^{v_0}(q^{v_0})$ by obstacles.

Therefore we can compute all the enclosed subspaces by repeatedly applying Algorithm 1 as shown in Algorithm 2.

In this algorithm, we first obtain the set of all obstacle polygons $\mathcal{P}_{\text{obs}}^v$ by *Polygon Intersection*. Then, search for the enclosed subspace containing the current node configuration — $\mathcal{C}_{\text{free}}^v(q^v)$ — from a starting polygon P_s , which is the nearest one to the node (Liu et al. 2020). Afterward, we compute all other enclosed subspaces in $\mathcal{C}_{\text{free}}^v$ by searching the boundary starting from any polygon that has not been used. Figure 13 shows two enclosed subspaces of node v_0 in a simple cubic truss. In total, there are 33 enclosed subspaces in $\mathcal{C}_{\text{free}}^{v_0}$ above the ground.

6.2 Topology Reconfiguration Actions

There are two topology reconfiguration actions: *Split* and *Merge*. A node constructed by six or more edge modules can be split into two separate nodes, and two separate nodes can merge into an individual node. These actions can significantly affect the motion of the involved nodes and there are several constraints when applying them. For the VTT shown in Figure 6, $\mathcal{C}_{\text{free}}^{v_0}(q^{v_0})$ that is the enclosed subspace containing the current location of node v_0 is shown in Figure 14a. This node can move to some locations outside truss but its motion is also blocked in some directions. The members attached with node v_1 blocked the motion of node v_0 on this side, and the plane formed by node v_2, v_3, v_6 , and v_7 also blocks the motion of v_0 due to: 1. collision avoidance with member (v_2, v_3) , (v_2, v_6) , (v_3, v_7) , and (v_6, v_7) ; 2. singularity avoidance that v_0 cannot move through the square

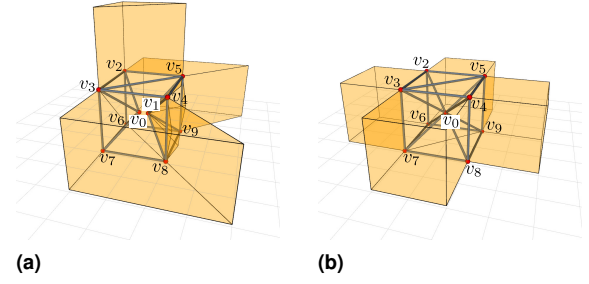


Figure 14. (a) Enclosed subspace $\mathcal{C}_{\text{free}}^{v_0}(q^{v_0})$ when v_0 and v_1 are separated; (b) Enclosed subspace $\mathcal{C}_{\text{free}}^{v_0}(q^{v_0})$ after merging v_1 with v_0 .

formed by v_2, v_3, v_6 , and v_7 . If merging v_1 and v_0 as v_0 shown in Figure 14b, $\mathcal{C}_{\text{free}}^{v_0}(q^{v_0})$ will be changed. The boundary originally blocked by members attached with node v_1 disappears because all members controlling v_0 and v_1 are combined into a single set. In addition, this Merge action increases the motion manipulability of node v_0 that can move through the square formed by v_2, v_3, v_6 , and v_7 . However, the side effect is that some originally reachable locations become not reachable, such as the space above the truss and around the member (v_4, v_8) . This is because E^{v_0} contains more members leading to the increase of the obstacle region of node v_0 .

When executing a *Split* action on a node, the basic requirement is that this node has to be constructed by at least six edge modules. In the process, we need to physically split a node into a pair and move them away. In order to guarantee motion controllability, singularity should be avoided during the whole process. In some situations, we need to carefully consider if it is feasible to execute this action. For example, when node v_0 is on the same plane with node v_2, v_3, v_6 , and v_7 shown in Figure 15a, it is not allowed to split node v_0 in the way shown in Figure 15b, because one of the newly generated nodes (v_0 in this case) will be in a singular configuration. In comparison, if node v_0 is outside the truss shown in Figure 16a, then it is feasible to apply the same *Split* action to generate two new nodes shown in Figure 16b. This constraint also applies for *Merge*. In Figure 15b, since node v_0 is in singular configuration, it is not allowed to merge v_1 with v_0 to become a new truss

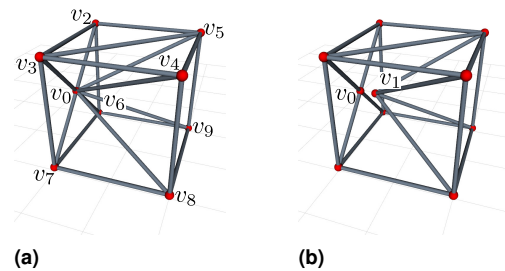


Figure 15. (a) Node v_0, v_2, v_3, v_6 , and v_7 are on the same plane. (b) Splitting node v_0 in this way to separate E^{v_0} into two sets is not valid, because node v_0 will be in singular configuration. Similarly, it is not valid to merge v_1 with v_0 .

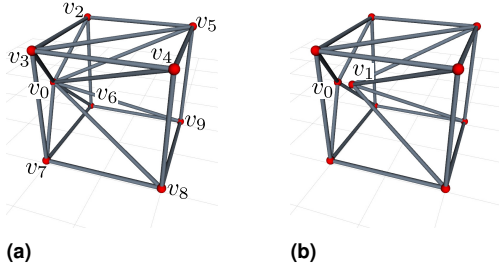


Figure 16. (a) Node v_0 is outside the truss. (b) It is possible to split node v_0 in this way to generate v_1 . Reversely, v_0 and v_1 can be merged.

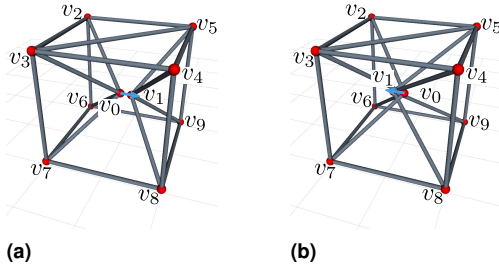


Figure 17. Split node v_0 into v_0 and v_1 : (a) a right way to move node v_1 away from node v_0 ; (b) a wrong way to move node v_1 away from node v_0 .

shown in Figure 15a. However, it is feasible to merge v_0 and v_1 in Figure 16b to become v_0 in Figure 16a.

After splitting a node, the members attached to this node are separated into two groups that can be controlled independently. However, we need to consider how to move the two newly generate nodes away from each other. In Figure 17a, after splitting v_0 into v_0 and v_1 , v_1 is moved to the right side of v_0 and this motion can separate these involved members without any collision. However, in Figure 17b, for the same Split action, v_1 is moved to the left side of v_0 and this motion is in fact not feasible because members will collide. This is also important for Merge. When merging two nodes, we first need to move them to some locations that are close to each other. If the new locations are not selected correctly, it is impossible to move them there and execute Merge action.

6.3 Topology Reconfiguration Planning

Given a VTT $G = (V, E)$ and the motion task that is to move node v from q_i^v to q_g^v , if q_i^v and q_g^v belong to the same enclosed subspace, then geometry reconfiguration planning is able to handle this problem by either the approach by Liu et al. (2020) or the approach introduced in Section 5.2. Otherwise, topology reconfiguration is needed. The node has to execute a sequence of Split and Merge in order to avoid collision with other members.

There are multiple ways for a node v to split into nodes v' and v'' as there are multiple ways to take the members into two groups, and it is straightforward to compute all possible ways to split E^v into two groups in which both sets contain at least three edge modules. Let \mathcal{A} be the set

of all possible ways to separate E^v into two groups. If v is split into v' and v'' , then E^v is separated into $E^{v'}$ and $E^{v''}$ accordingly. This split process is denoted as $(E^{v'}, E^{v''})$. Not all possible ways in \mathcal{A} can be applied on node v . Given a valid VTT $G = (V, E)$ and a node v , a Split action can be encoded as a tuple $(E^{v'}, E^{v''}, q_s^{v'}, q_s^{v''})$ where v' and v'' are the newly generated node after splitting, and $q_s^{v'}$ and $q_s^{v''}$ are the locations of these two new nodes. For simplicity, $q_s^{v'} = q^v$ and v'' is moved away from v' along a unit vector d_v so that there is no collision introduced after this process. The direction of d_v is determined by $q_s^{v'}$ (the current location of v') and $\mathcal{N}_G(v')$ (the neighbors of v'), and can be derived by normalizing the following vector

$$\sum_{\hat{v} \in \mathcal{N}_G(v')} \frac{q_s^{v'} - q^{\hat{v}}}{\|q_s^{v'} - q^{\hat{v}}\|} \quad (15)$$

and the distance moved along vector d_v can be tried iteratively until there is no collision in this VTT. In addition to the collision-free requirement, the resulted VTT should satisfy all other hardware constraints described in Section 4.2 after splitting, and let $V_C = \{v', v''\}$ when checking the motion manipulability by Eq. 12.

Given a location of node v and one way to split E^v into $E^{v'}$ and $E^{v''}$, Function **ComputeSplitAction** is used to check and compute this Split action. In this function, G is the given VTT, $a \in \mathcal{A}$ is a possible split way, and D , ΔD , and D_{\max} are three parameters. Function **VTTValidation** returns true if a given VTT satisfies all hardware constraints, otherwise returns false. Function **VTTCollisionCheck** returns false if there is no collision among all members, otherwise returns true. The basic idea is to move v'' gradually away from v' until a valid VTT is found. The maximum distance between v' and v'' for searching is D_{\max} that should be a small value. Within this small range, member collision

Function ComputeSplitAction($G, q^v, a \in \mathcal{A}$)

Data: $D, \Delta D, D_{\max}$

```

1 Move node  $v$  to  $q^v$ ;
2 if VTTValidation( $G$ ) = False then
3   return Null;
4 end
5 Split node  $v$  into  $v'$  and  $v''$  according to  $a \in \mathcal{A}$ ;
6  $q_s^{v'} \leftarrow q^v, q_s^{v''} \leftarrow q^v$ ;
7 Compute  $d_v$ ;
8 repeat
9    $q_s^{v''} = q^v + Dd_v$ ;
10  Move node  $v''$  to  $q_s^{v''}$ ;
11  if VTTCollisionCheck( $G$ ) = True then
12     $D \leftarrow (D + \Delta D)d_v$ ;
13  else
14    if VTTValidation( $G$ ) = True then
15      return  $(E^{v'}, E^{v''}, q_s^{v'}, q_s^{v''})$ ;
16    else
17      return Null;
18    end
19  end
20 until  $D \leq D_{\max}$ ;
21 return Null;
```

is a more significant constraint, such as the case shown in Figure 17b. Hence initially only checking collision among members, and once a collision-free location for v'' is found, check other hardware constraints. Reversely, if merging v' and v'' as v at a location q^v , with this computed Split action $(E^{v'}, E^{v''}, q_s^{v'}, q_s^{v''})$, we can first check if $q_s^{v'} = q^v \in C_{\text{free}}^v(q^{v'})$ and $q_s^{v''} \in C_{\text{free}}^v(q^{v''})$, and if true, move v' to $q_s^{v'}$ and move v'' to $q_s^{v''}$, and then merge them at q^v .

Given q^v , the current position of node v , and $C_{\text{free}}^v = \{C_{\text{free}}^v | t = 1, 2, \dots, T\}$ that contains T enclosed subspaces in the free space of node v , apply a valid Split action on this node to separate E^v into $E^{v'}$ and $E^{v''}$ and generate two new nodes v' and v'' . $q^{v'}$ and $q^{v''}$ are the locations of v' and v'' , and $C_{\text{free}}^{v'}(q^{v'})$ and $C_{\text{free}}^{v''}(q^{v''})$ can be computed accordingly. Assuming there is a position $q \in C_{\text{free}}^v$ where node v can also be split in the same way (E^v can be separated into $E^{v'}$ and $E^{v''}$ with Split action $(E^{v'}, E^{v''}, q_s^{v'}, q_s^{v''})$), if $q_s^{v'} \in C_{\text{free}}^v(q^{v'})$ and $q_s^{v''} \in C_{\text{free}}^v(q^{v''})$, namely v' and v'' can navigate to $q_s^{v'}$ and $q_s^{v''}$ respectively and merge at q , then this node v can navigate from $C_{\text{free}}^v(q^v)$ to C_{free}^v by a pair of Split and Merge actions, and these two enclosed subspaces can be connected under this action pair. This is the transition model when applying topology reconfiguration actions. From Section 6.2, it is shown that the possible ways to split a node are highly dependent on the location of the node, and the resulted enclosed subspaces of the newly generated nodes can be very different when splitting the node at different locations. Hence, there are two phases in the topology reconfiguration planning: *sample generation* and *graph search*.

In *sample generation*, multiple samples are generated for every enclosed subspace. These samples are expected to provide valid Split actions as many as possible and also cover the space as much as possible. We introduce Algorithm 3 to sample a given enclosed subspace. \mathcal{S} is the set containing all generated valid samples and $\mathcal{A}^{\mathcal{S}}$ stores the Split actions for every sample. N_{max} is the maximum number of samples for a given enclosed subspace C_{free}^v and it is determined by the size of the space: a larger space is expected to have more samples. In our setup, we find the range of a given space along x , y , and z axis denoted as x_{range} , y_{range} , and z_{range} respectively, then N_{max} is simply $\lceil \sqrt{x_{\text{range}}^2 + y_{\text{range}}^2 + z_{\text{range}}^2} / d_{\text{min}} \rceil$ in which d_{min} is the minimum distance between every pair of samples. K is the maximum number of iterations set by users and can be related to N_{max} . For each iteration, we first randomly generate a sample q_{rand} that is inside the given enclosed subspace, then find all valid Split actions stored in $\mathcal{A}_{\text{valid}}$ (Line 6—13). Then find all previous valid samples that are close to q_{rand} (Line 14). If q_{rand} is far from all previous valid samples and the size of \mathcal{S} is less than N_{max} , add this new sample and store its valid Split actions (Line 15—17). If q_{rand} is close to some previous valid samples, there are two cases for consideration. If this new sample provides all possible Split actions, then remove all valid close samples and only keep this new sample for this area since this is the best option (Line 19—24). Otherwise, we check two conditions: 1. whether there exists any valid close sample that has fewer number of valid Split actions than q_{rand} ; 2. whether the new sample q_{rand} introduces any new

Algorithm 3: Sample Generation

Input: $C_{\text{free}}^v, G, \mathcal{A}$
Output: $\mathcal{S}, \mathcal{A}^{\mathcal{S}}$

```

1  $\mathcal{S} \leftarrow \emptyset$ ;
2 Initialize an empty map  $\mathcal{A}^{\mathcal{S}}$ ;
3 Initialize  $d_{\text{min}}$ ;
4  $N_{\text{max}} \leftarrow \text{SampleNumber}(C_{\text{free}}^v)$ ;
5 for  $k = 1$  to  $K$  do
6    $\mathcal{A}_{\text{valid}} \leftarrow \emptyset$ ;
7    $q_{\text{rand}} \leftarrow \text{RandomPosition}(C_{\text{free}}^v)$ ;
8   foreach  $a \in \mathcal{A}$  do
9      $\hat{a} = \text{ComputeSplitAction}(G, q, a)$ ;
10    if  $\hat{a}$  is not Null then
11       $\mathcal{A}_{\text{valid}} = \mathcal{A}_{\text{valid}} \cup \{\hat{a}\}$ ;
12    end
13  end
14   $\mathcal{S}_{\text{close}} \leftarrow \{q | q \in \mathcal{S} \wedge \|q - q_{\text{rand}}\| \leq d_{\text{min}}\}$ ;
15  if  $\mathcal{S}_{\text{close}} = \emptyset \wedge |\mathcal{S}| < N_{\text{max}}$  then
16     $\mathcal{S} \leftarrow \mathcal{S} \cup \{q_{\text{rand}}\}$ ;
17     $\mathcal{A}^{\mathcal{S}}[q] = \mathcal{A}_{\text{valid}}$ ;
18  else if  $\mathcal{S}_{\text{close}} \neq \emptyset \wedge |\mathcal{S}| < N_{\text{max}}$  then
19    if  $|\mathcal{A}_{\text{valid}}| = |\mathcal{A}|$  then
20      foreach  $q \in \mathcal{S}_{\text{close}}$  do
21         $\text{del } \mathcal{A}^{\mathcal{S}}[q]$ ;
22      end
23       $\mathcal{S} \leftarrow \mathcal{S} \setminus \mathcal{S}_{\text{close}} + \{q_{\text{rand}}\}$ ;
24       $\mathcal{A}^{\mathcal{S}}[q_{\text{rand}}] = \mathcal{A}_{\text{valid}}$ ;
25    else
26      UpdateFlag  $\leftarrow$  False;
27      foreach  $q \in \mathcal{S}_{\text{close}}$  do
28        if  $\mathcal{A}^{\mathcal{S}}[q] \subset \mathcal{A}_{\text{valid}}$  then
29           $\text{del } \mathcal{A}^{\mathcal{S}}[q]$ ;
30           $\mathcal{S} \leftarrow \mathcal{S} \setminus \{q\}$ ;
31           $N_{\text{max}} \leftarrow N_{\text{max}} - 1$ ;
32          UpdateFlag  $\leftarrow$  True;
33        else if  $|\mathcal{A}_{\text{valid}} \setminus \mathcal{A}^{\mathcal{S}}[q]| \neq \emptyset$  then
34          UpdateFlag  $\leftarrow$  True;
35        end
36      end
37      if UpdateFlag = True then
38         $\mathcal{S} \leftarrow \mathcal{S} + \{q_{\text{rand}}\}$ ;
39         $\mathcal{A}^{\mathcal{S}}[q_{\text{rand}}] = \mathcal{A}_{\text{valid}}$ ;
40         $N_{\text{max}} \leftarrow N_{\text{max}} + 1$ ;
41      end
42    end
43  end
44 end

```

Split actions compared with all valid close samples. If the first condition is true, remove the old sample and add the new sample to \mathcal{S} . If the second condition is true, add the new sample to \mathcal{S} (Line: 26—41). We run Algorithm 3 for every enclosed subspace to generate enough samples, and then add q_i^v (the initial location of node v) to the sample set of $C_{\text{free}}^v(q_i^v)$ and add q_g^v (the goal location of node v) to the sample set of $C_{\text{free}}^v(q_g^v)$. After *sample generation* phase, $\mathcal{C}\mathcal{S}$ and the corresponding Split actions for all samples $\mathcal{C}\mathcal{A}^{\mathcal{S}}$ are obtained for every enclosed subspace $\mathcal{C} \in C_{\text{free}}^v$.

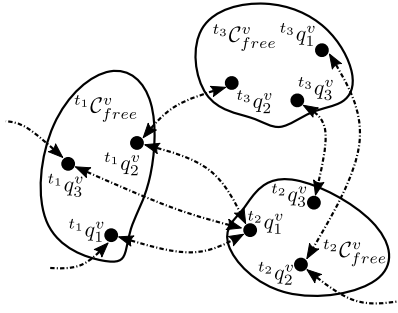


Figure 18. Topology connections among three enclosed subspaces of node v .

Then we can enter the *graph search* phase to generate a sequence of topology reconfiguration actions. With the transition model discussed before, a graph search algorithm can be applied to compute a sequence of enclosed subspaces starting from $C_{\text{free}}^v(q_i^v)$ to $C_{\text{free}}^v(q_g^v)$ while exploring the topology connections among these enclosed subspaces. An example is shown in Figure 18. Here, the graph has enclosed subspaces as vertices. An edge in this graph connecting two enclosed subspaces denotes that node v can move from a sample in one enclosed subspace to a sample in the other. The graph is built from $C_{\text{free}}^v(q^v)$, grows as valid transitions among enclosed subspaces are found, and stops when the enclosed subspace containing q_g^v is visited. A graph search algorithm designed based on Dijkstra's framework is shown in Algorithm 4.

Line 1 — 5: If q_i^v and q_g^v are in the same enclosed subspace, then no topology reconfiguration is needed. Otherwise, we make two sets \mathcal{Q} and $\bar{\mathcal{Q}}$ where \mathcal{Q} contains all newly checked or non-visited enclosed subspaces and $\bar{\mathcal{Q}}$ contains all visited enclosed subspaces. The size of these two sets will change as the algorithm explores C_{free}^v . Initially, only the enclosed subspace containing q_i^v that is $C_{\text{free}}^v(q_i^v)$ and the enclosed subspace containing q_g^v that is $C_{\text{free}}^v(q_g^v)$ are in \mathcal{Q} , and the algorithm starts with $C_{\text{free}}^v(q_i^v)$. The value $g(\mathcal{C})$ is the cost of the path from q_i^v to the enclosed subspace \mathcal{C} , so $g(C_{\text{free}}^v(q_i^v)) = 0$ and $g(C_{\text{free}}^v(q_g^v)) = \infty$ in the beginning.

Line 7 — 9: Every iteration starts with the enclosed subspace that has the lowest cost $g(\mathcal{C})$ in \mathcal{Q} . At the beginning, $C_{\text{free}}^v(q_i^v)$ has the lowest cost. After selecting an enclosed subspace, update \mathcal{Q} and $\bar{\mathcal{Q}}$.

Line 10 — 26: Iterate every enclosed subspace \mathcal{C} except $\bar{\mathcal{C}}$ in C_{free}^v and check if it is already visited. If so, then this potential transition is not a new transition. Otherwise, check if there exists a valid motion to move the node from any sample in $\bar{\mathcal{C}}$ that is the enclosed subspace with the lowest cost to any sample in \mathcal{C} . If this is true, then there are two cases: this subspace is not checked for the first time namely that there is already a connection between this enclosed subspace and another enclosed subspace, or this subspace has never been checked which means they have no connection before. For the first case, we need to check whether its cost needs to be updated. $c(\bar{\mathcal{C}}_q, \mathcal{C}_q)$ is the cost of the motion from $\bar{\mathcal{C}}_q$ to \mathcal{C}_q . This cost can be related to the estimated distance or other factors. In our setup, all valid motions from one enclosed subspace to another one have the same cost. If its cost is updated, then its parent $p(\mathcal{C})$ should also be updated accordingly. For the second case, initialize the cost

Algorithm 4: Topology Reconfiguration Planning

Input: $G, q_i^v, q_g^v, C_{\text{free}}^v, \{(\mathcal{C}^v, \mathcal{C}^{\mathcal{A}}) | \mathcal{C} \in C_{\text{free}}^v\}$

Output: Tree of enclosed subspaces p

```

1 if  $C_{\text{free}}^v(q_i^v) = C_{\text{free}}^v(q_g^v)$  then
2   return Null;
3 end
4  $\mathcal{Q} \leftarrow \{C_{\text{free}}^v(q_i^v), C_{\text{free}}^v(q_g^v)\}, \bar{\mathcal{Q}} \leftarrow \emptyset;$ 
5  $g(C_{\text{free}}^v(q_i^v)) \leftarrow 0, g(C_{\text{free}}^v(q_g^v)) \leftarrow \infty;$ 
6 while  $C_{\text{free}}^v(q_g^v) \in \mathcal{Q}$  do
7    $\bar{\mathcal{C}} \leftarrow \arg \min_{\mathcal{C} \in \mathcal{Q}} g(\mathcal{C});$ 
8    $\mathcal{Q} \leftarrow \mathcal{Q} \setminus \{\bar{\mathcal{C}}\};$ 
9    $\bar{\mathcal{Q}} \leftarrow \bar{\mathcal{Q}} \cup \{\bar{\mathcal{C}}\};$ 
10  foreach  $\mathcal{C} \in C_{\text{free}}^v \setminus \{\bar{\mathcal{C}}\} \wedge \mathcal{C} \notin \bar{\mathcal{Q}}$  do
11    foreach  $(\bar{\mathcal{C}}_q, \mathcal{C}_q) \in \bar{\mathcal{C}}\mathcal{S} \times \mathcal{C}\mathcal{S}$  do
12      if ValidMotion( $\bar{\mathcal{C}}_q, \mathcal{C}_q$ ) = True then
13        if  $\mathcal{C} \in \mathcal{Q}$  then
14          if  $g(\bar{\mathcal{C}}) + c(\bar{\mathcal{C}}_q, \mathcal{C}_q) < g(\mathcal{C})$  then
15             $g(\mathcal{C}) \leftarrow g(\bar{\mathcal{C}}) + c(\bar{\mathcal{C}}_q, \mathcal{C}_q);$ 
16             $p(\mathcal{C}) \leftarrow \bar{\mathcal{C}};$ 
17          end
18        else
19           $\mathcal{Q} \leftarrow \mathcal{Q} \cup \{\mathcal{C}\};$ 
20           $g(\mathcal{C}) \leftarrow g(\bar{\mathcal{C}}) + c(\bar{\mathcal{C}}_q, \mathcal{C}_q);$ 
21           $p(\mathcal{C}) \leftarrow \bar{\mathcal{C}};$ 
22        end
23      end
24    break;
25  end
26 end
27 end

```

and the parent of this newly checked enclosed subspace, and update set \mathcal{Q} . There can be multiple ways to transit between two enclosed subspaces. For example, there are two edges between $t_2C_{\text{free}}^v$ and $t_3C_{\text{free}}^v$ shown in Figure 18. In our setup, we just keep the first one being found. Since $\bar{\mathcal{C}}\mathcal{S}$ and $\mathcal{C}\mathcal{S}$ are randomly generated, it is possible that the condition in Line 12 is failed although there does exist $\bar{\mathcal{C}}_q$ and \mathcal{C}_q that can pass this condition.

Once $C_{\text{free}}^v(q_g^v)$ is visited, the algorithm ends. With p , a tree with visited enclosed subspaces as vertices, it is straightforward to find the optimal path connecting $C_{\text{free}}^v(q_i^v)$ and $C_{\text{free}}^v(q_g^v)$ as well as all the samples the node need to traverse. For example, in Figure 18, when node v traverses from $t_1q_1^v$ to $t_3q_1^v$, it first moves to $t_1q_2^v$, then Split and Merge at $t_3q_2^v$, and finally move to $t_3q_1^v$. Moving a node inside one of its enclosed subspaces can be solved easily by geometry reconfiguration planning. After splitting the node into a pair, we can also apply geometry reconfiguration planning to move them to the computed positions in the next enclosed subspace for merging.

7 Locomotion

Unlike the previous control for reconfiguration, the center of mass during locomotion moves over a large range by

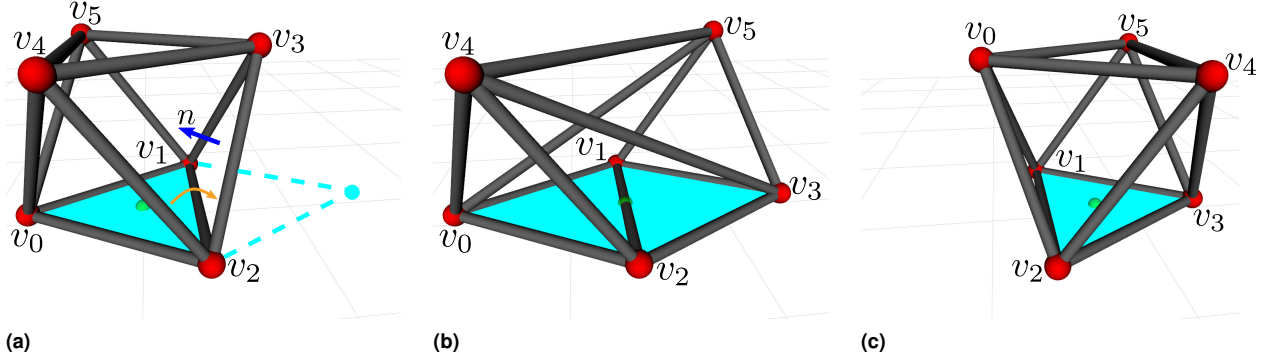


Figure 19. A VTT in octahedron configuration executes a single rolling locomotion step. (a) Initially node v_0 , v_1 , and v_2 forms the support polygon shown in blue, and the center of mass projected onto the ground (green dot) is within this support polygon. The truss wants to roll from its current support polygon to an adjacent support polygon formed by node v_1 , v_2 , and the new tipping location. (b) v_3 and v_5 are moved so that the support polygon is expanded and the center of mass projected onto the ground is on the member (v_1, v_2) . (c) v_0 and v_4 are moved to the destination to finish this locomotion step, and the center of mass projects onto the ground is within the new support polygon formed by node v_1 , v_2 , and v_3 .

continuously interacting with the environment. In a rolling locomotion step, a VTT rolls from one support polygon to an adjacent support polygon (Figure 19a). In this process, it is useful to maintain statically stable locomotion to prevent the system from receiving impacts from the ground as repeated impacts may damage the reconfiguration nodes. Due to this requirement, a rolling locomotion step has to be manually divided into several phases to have control over the center of mass (Park et al. 2020; Usevitch et al. 2020). Our approach can deal with this issue automatically while planning the motion of nodes that need to be moved. A high-level path planner can generate a support polygon trajectory given an environment and a locomotion task, and the locomotion planner can ensure that the truss can follow this support polygon trajectory without violating constraints and receiving impacts from the ground.

7.1 Truss Polyhedron

The boundary representation of a VTT is modeled as a convex polyhedron which can be either defined initially or obtained from the set of node positions by computing the convex hull of them using existing computational geometry algorithms, such as Quickhull (Barber et al. 1996). Given a VTT $G = (V, E)$, its polyhedron representation can be fully defined as $P^G = (E^G, F^G)$ in which F^G is the set of facets forming the boundary of this VTT and E^G is the set of edges forming all facets, namely each facet is composed of multiple edge members in E^G and each edge of E^G is incident to two facets. For example, the boundary representation of the VTT in Figure 19a is an octahedron in which edge (v_1, v_2) is incident to facet (v_1, v_2, v_3) and facet (v_0, v_1, v_2) . In this example, all edges are contained in its polyhedron representation. However, for the VTT in Figure 13, v_0 and its corresponding edges in E^{v_0} are not involved in its polyhedron representation.

Suppose the set of edges forming a facet $f \in F^G$ is $E_f^G \subset E^G$, and $\forall e \in E_f^G$, the other incident facet of edge e is $f^e \in F^G$. Every facet can be a support polygon as long as all of its vertices are on the ground. Assume $f \in F^G$ is the current support polygon and a single rolling locomotion step

is equivalent to rotating the truss with respect to an edge of this facet $e \in E_f^G$ until the other incident facet of this edge f^e becomes the new support polygon. An example of this process is shown in Figure 19. Initially facet $f = (v_0, v_1, v_2)$ is the support polygon, and the other incident facet of edge $e = (v_1, v_2) \in E_f^G$ is $f^e = (v_1, v_2, v_3)$. If we want to control the robot to do locomotion from Figure 19a to Figure 19c, the result of this process is equivalent to rotating the truss with respect the fixed edge $e = (v_1, v_2)$ until the support polygon becomes f^e . This means the input command for each locomotion step can be simply an edge of the current support polygon, e.g. (v_1, v_2) for the scenario in Figure 19.

7.2 Locomotion Planning

Given a VTT $G = (V, E)$, its truss polyhedron model $P^G = (E^G, F^G)$ and its current support polygon $f \in F^G$ can be derived. Given a locomotion command $e \in f$, we can find f^e and compute its normal vector n_{f^e} pointing inwards P^G (e.g. vector n for facet (v_1, v_2, v_3) in Figure 19a), then the rotation angle α between n_{f^e} and the normal vector of the ground $[0, 0, 1]^T$ is simply

$$\alpha = \arccos \left(\frac{n_{f^e} \bullet [0, 0, 1]^T}{\|n_{f^e}\|} \right) \quad (16)$$

The rotation axis is along edge $e = (v_1^e, v_2^e)$ and its direction can be easily determined by the right-hand rule. For the example shown in Figure 19, the rotation axis is simply $\frac{q^{v_1} - q^{v_2}}{\|q^{v_1} - q^{v_2}\|}$, namely the unit vector pointing from node v_2 to node v_1 . Assume the rotation axis is pointing from v_1^e to v_2^e , then the rotation angle and the rotation axis determine a rotation matrix R^e , and for every node $v \in V \setminus \{v_1, v_2\}$ during this locomotion process, its initial position q_i^v is known as q^v and its goal position q_g^v can be derived as

$$q_g^v = R^e(q^v - q^{v_1^e}) + q^{v_1^e} \quad (17)$$

Then we can make use of the approach presented in Section 5.3 to plan the motion for all of these involved nodes to execute the locomotion step. Due to the stability constraint that at least three nodes need to contact the ground to form

a support polygon and the center of mass represented on the ground has to be within this support polygon, the planner will automatically move nodes first to expand the support polygon so that the center of mass can be moved in a larger range. An example of this non-impact rolling locomotion planning result is shown in Figure 19. In this task, the initial support polygon is facet (v_0, v_1, v_2) and we want to roll the truss so that facet (v_1, v_2, v_3) becomes the new support polygon. The locomotion command is simply (v_1, v_2) , the rotation axis and the rotation angle can be computed as mentioned, and four nodes $(v_0, v_3, v_4, \text{ and } v_5)$ have to move to new locations which can be derived from Eq. (17). Because of the stability constraint, node v_0 cannot be moved at the beginning, or the robot won't be stable since there will be no support polygon. The planner chooses to move v_3 and v_5 first to expand the support polygon which is formed by node v_0, v_1, v_2 , and v_3 , and the center of mass is moved towards the target support polygon (Figure 19b). The center of mass projected onto the ground is always within the initial support polygon. After the support polygon is expanded, v_0 and v_4 are moved, and, in the meantime, the projected center of mass enters the target support polygon (Figure 19c).

8 Test Scenarios

The motion planning framework is implemented in C++. Four example scenarios were conducted to measure the effectiveness of our approach. The performance of the reconfiguration framework is compared with the approach by Jeong et al. (2018) and Liu and Yim (2019). The performance of the locomotion framework is compared with the approach by Park et al. (2020) and Usevitch et al. (2020). These experiments are also tested under different constraints

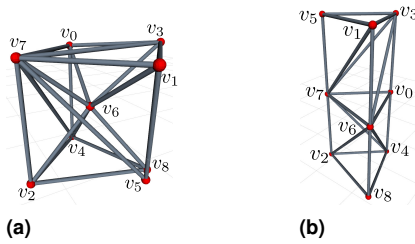


Figure 20. The motion task is to change the shape of a VTT from (a) a cubic truss for rolling locomotion to (b) a tower truss for shoring.

and with different parameters to show the universality of our framework. All tests run on a laptop computer (Intel Core i7-8750H CPU, 16GB RAM) and the workspace is a cuboid.

8.1 Geometry Reconfiguration

The geometry reconfiguration planning test changes the cube shape of a VTT, Figure 20a, to a tower shape, Figure 20b. This VTT is composed of 21 members with initial positions of nodes listed in the following

$$\begin{aligned} q^{v_0} &= [-1.605, -0.771, 2.075]^T \\ q^{v_1} &= [0.7779, -0.7642, 2.075]^T \\ q^{v_2} &= [-0.4756, -2.022, 0.075]^T \\ q^{v_3} &= [-0.4142, 0.4228, 2.175]^T \\ q^{v_4} &= [-1.605, -0.771, 0.075]^T \\ q^{v_5} &= [0.3819, -0.3707, 0.125]^T \\ q^{v_6} &= [-0.4314, -0.9559, 1.2321]^T \\ q^{v_7} &= [-0.4756, -2.022, 2.075]^T \\ q^{v_8} &= [0.1819, -0.1707, 0.075]^T \end{aligned}$$

The constraints for this task are $\bar{L}_{\min} = 1.0 \text{ m}$, $\bar{L}_{\max} = 3.5 \text{ m}$, $\bar{\theta}_{\min} = 0.3 \text{ rad}$, and $\bar{\mu}_{\min} = 0.1$.

Four nodes v_1, v_3, v_5 , and v_6 are involved in this motion task and their goal positions in the tower VTT are $q_g^{v_1} = [0.18, -0.17, 4.13]^T$, $q_g^{v_3} = [-1.61, -0.77, 4.08]^T$, $q_g^{v_5} = [-0.48, -2.02, 4.08]^T$, and $q_g^{v_6} = [0.18, -0.17, 2.13]^T$. These four nodes are separated into two groups $\{v_3, v_5\}$ and $\{v_1, v_6\}$ which is randomly selected. We first compute $\hat{\mathcal{C}}_{\text{free}}^{v_3}(q_i^{v_3})$ and $\hat{\mathcal{C}}_{\text{free}}^{v_5}(q_i^{v_5})$, and then do planning for these two nodes. The motion of node v_3 and v_5 is shown in Figure 21. Most of the obstacle region in this step is surrounded by the subspace $\hat{\mathcal{C}}_{\text{free}}^{v_3}(q_i^{v_3})$ and $\hat{\mathcal{C}}_{\text{free}}^{v_5}(q_i^{v_5})$, hence it is easier for them to extend outwards first in order to navigate to the goal positions. This motion process moves the projected center of mass towards one edge of the support polygon but the planner can constrain the projected center of mass within the support polygon. After planning for v_3 and v_5 , the truss is updated, and $\hat{\mathcal{C}}_{\text{free}}^{v_1}(q_i^{v_1})$ and $\hat{\mathcal{C}}_{\text{free}}^{v_6}(q_i^{v_6})$ are computed accordingly. Finally the planning for v_1 and v_6 finishes this motion task with the result shown in Figure 22. For v_1 and v_6 in this updated truss, the enclosed subspace $\hat{\mathcal{C}}_{\text{free}}^{v_1}(q_i^{v_1})$ and $\hat{\mathcal{C}}_{\text{free}}^{v_6}(q_i^{v_6})$ almost covers the whole workspace so it is also easy to navigate to the goal positions. The minimum length (L_{\min}) and the maximum length (L_{\max}) of all moving edge modules, the minimum angle between every pair of edge

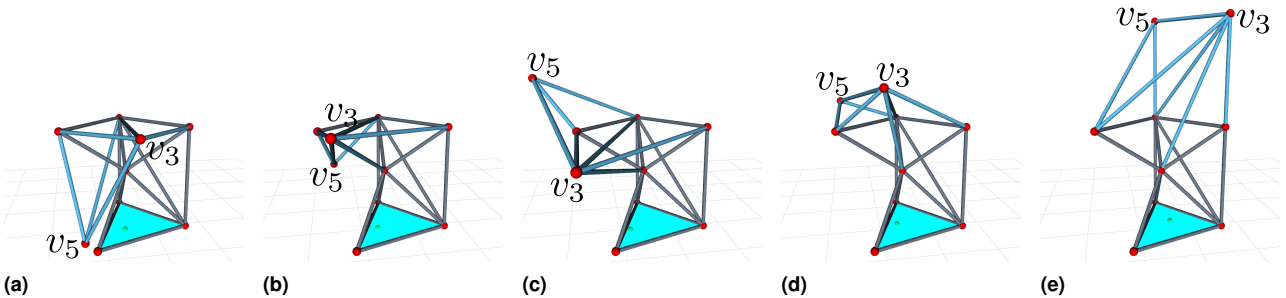


Figure 21. v_3 and v_5 firstly extend outwards, and then move upward to their goal positions. The support polygon is formed by three nodes (v_2, v_4, v_5) on the ground shown as a triangle (▲) and the green dot (●) is the center of mass represented on the ground.

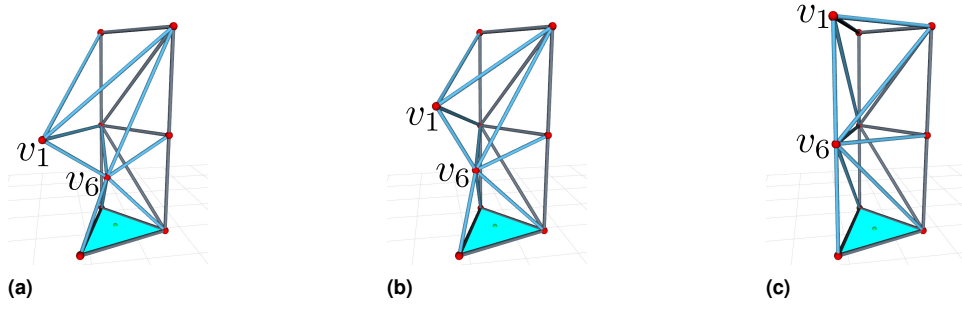


Figure 22. v_1 and v_6 can navigate to their goal positions easily since $\hat{\mathcal{C}}_{\text{free}}^{v_1}(q_i^{v_1})$ and $\hat{\mathcal{C}}_{\text{free}}^{v_6}(q_i^{v_6})$ almost cover the whole workspace.

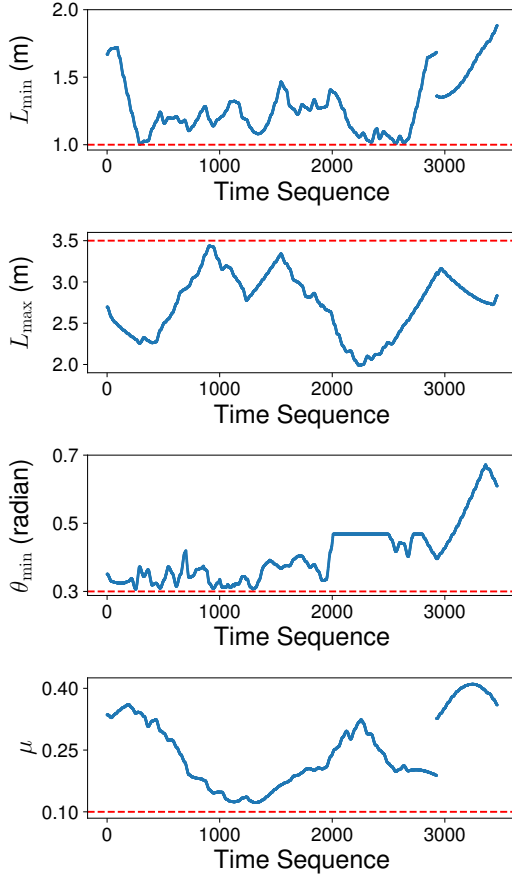


Figure 23. The minimum length (L_{\min}) and the maximum length (L_{\max}) of all moving edge modules, the minimum angle between every pair of edge modules (θ_{\min}), and the motion manipulability (μ) are measured throughout the geometry reconfiguration process in Figure 21 and Figure 22.

modules (θ_{\min}), and the motion manipulability (μ) are shown in Figure 23. Note that L_{\min} , L_{\max} , and μ are not necessarily to be continuous because nodes that are under control are changing. This motion task is also demonstrated by Jeong et al. (2018) using the retraction-based RRT algorithm. This algorithm cannot solve this motion planning task in 100 trials unless an intermediate waypoint is manually specified to mitigate the narrow passage issue. The success rate for the planning from the initial to the waypoint is 99% and 98% from the waypoint to the goal. In comparison, our algorithm doesn't need any additional waypoints, and we did 1000

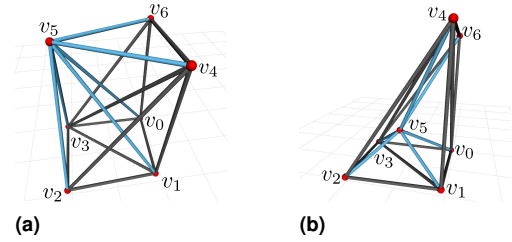


Figure 24. (a) A VTT is constructed from 18 edge modules with 6 nodes. (b) The goal is to move node v_5 from its initial position to a position inside the truss.

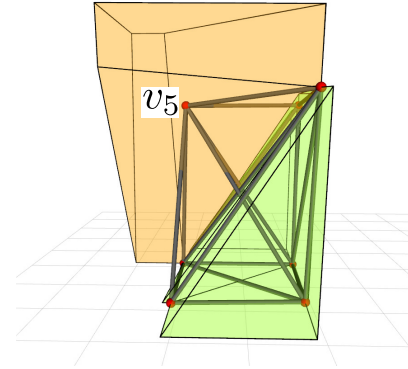


Figure 25. $\mathcal{C}_{\text{free}}^{v_5}(q_i^{v_5})$ is the yellow space on the upper left and $\mathcal{C}_{\text{free}}^{v_5}(q_g^{v_5})$ is the green space on the lower right. They are not connected and separated by the obstacle region generated from edge (v_3, v_4) .

trials and the mean running time is 4.158 s with a standard deviation of 1.952 s and the success rate is 100%.

8.2 Topology Reconfiguration

8.2.1 Scenario 1 The VTT configuration used for this topology reconfiguration example is shown in Figure 24a with the following nodes' positions

$$\begin{aligned} q^{v_0} &= [0.05, 0, 0.075]^T & q^{v_1} &= [0.1, 1.8, 0.075]^T \\ q^{v_2} &= [2.1, 1.9, 0.075]^T & q^{v_3} &= [2.1, 0, 0.075]^T \\ q^{v_4} &= [0, 2.1, 3.225]^T & q^{v_5} &= [1.95, 0.9, 3]^T \\ q^{v_6} &= [0, 0, 3.025]^T \end{aligned}$$

The constraints for this task are $\bar{L}_{\min} = 1.0$ m, $\bar{L}_{\max} = 5.0$ m, $\bar{\theta}_{\min} = 0.2$ rad, and $\bar{\mu}_{\min} = 0.1$.

The motion task is to move v_5 from its initial position $q_i^{v_5} = [1.95, 0.9, 3]^T$ to a goal position $q_g^{v_5} = [1, 1.2, 0.9]^T$

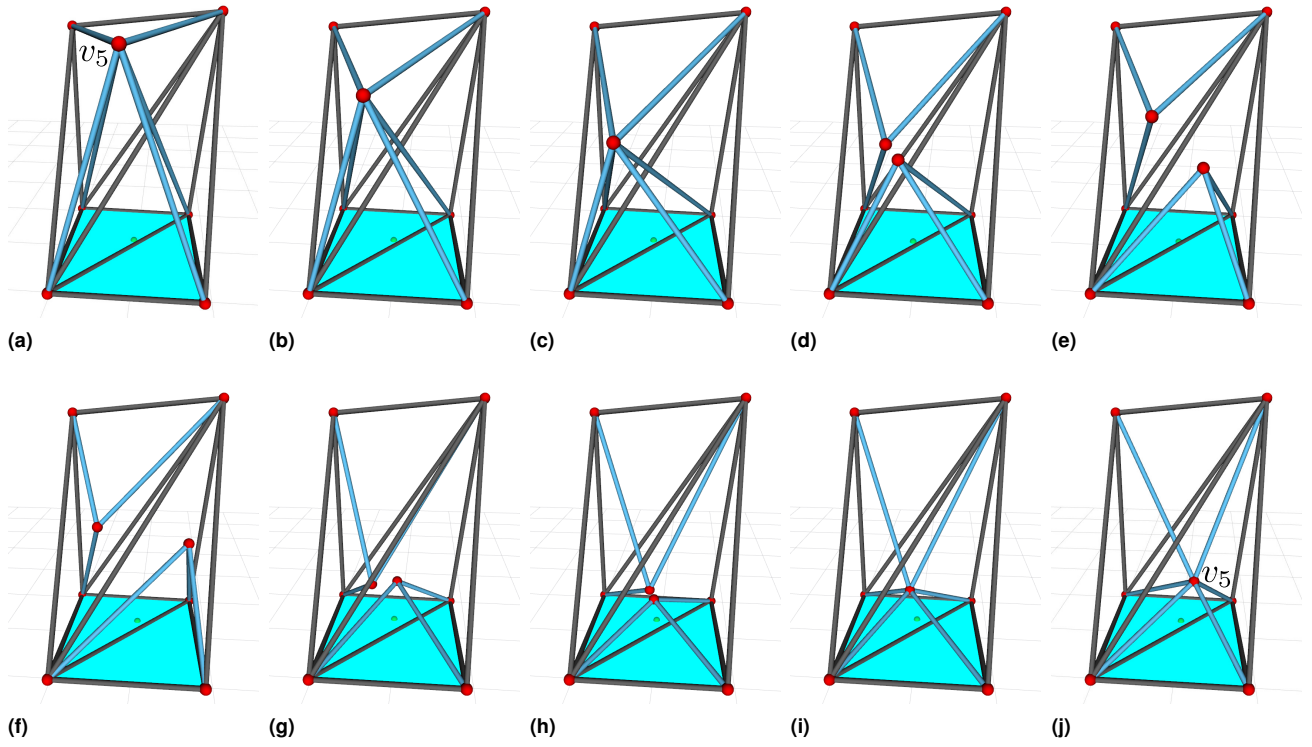


Figure 26. The sequence to move v_5 from $q_i^{v_5}$ to $q_g^{v_5}$ is shown. (a) — (c) First move v_5 to a new location. (d) Split v_5 into a pair. (e) — (h) Move these two newly generated nodes in different directions to go around the edge module (v_3, v_4) . (i) — (j) Merge them into an individual node and move this node to $q_g^{v_5}$.

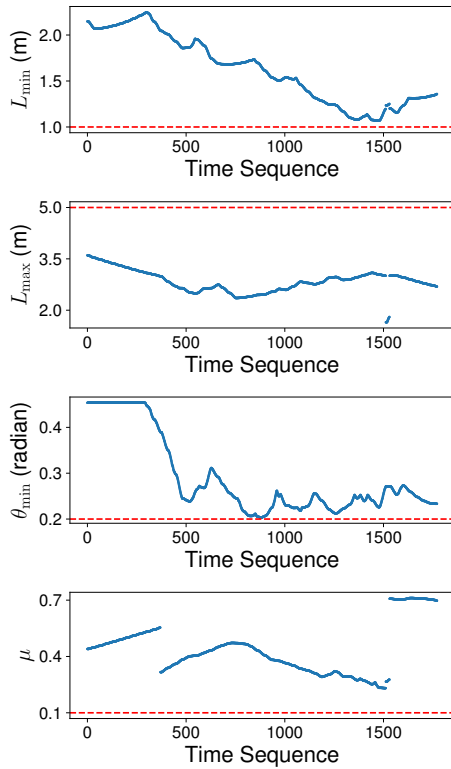


Figure 27. The minimum length (L_{\min}) and the maximum length (L_{\max}) of all moving edge modules, the minimum angle between every pair of edge modules (θ_{\min}), and the motion manipulability (μ) are measured throughout the topology reconfiguration process in Figure 26.

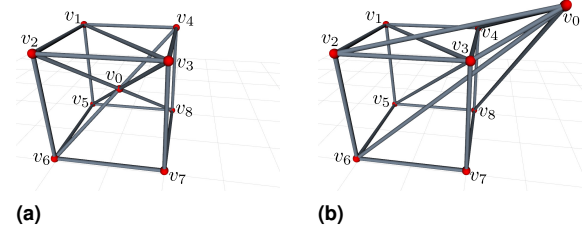


Figure 28. (a) A VTT is constructed from 19 members with 9 nodes. (b) The task is to move v_0 from its initial position to a position outside the cubic truss.

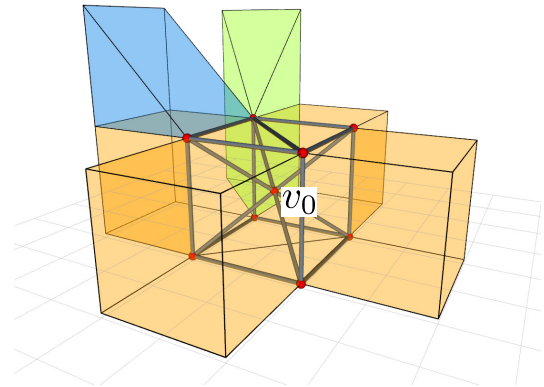


Figure 29. v has to move from $C_{\text{free}}^v(q_i^v)$ that is the yellow enclosed subspace to the green enclosed subspace, and then $C_{\text{free}}^v(q_g^v)$ that is the blue enclosed subspace.

(Figure 24b). This motion cannot be executed with only geometry reconfiguration because $\mathcal{C}_{\text{free}}^{v_5}(q_i^{v_5})$ and $\mathcal{C}_{\text{free}}^{v_5}(q_g^{v_5})$ shown in Figure 25 are separated by the obstacle region generated from edge module (v_3, v_4) . For this task, the minimum distance between two nodes is $d_{\min} = 1.0$ m and N_{\max} is constrained to be greater than or equal to 3, namely it is expected to have at least 3 samples for every enclosed subspace, and the maximum number of iterations $K = 5N_{\max}$.

With our topology reconfiguration planning algorithm (Algorithm 4), one pair of Split and Merge actions is sufficient. v_5 is moved to a new location, then split into a pair of nodes (v_5' and v_5'') so that both of these two newly generated nodes can navigate to $\mathcal{C}_{\text{free}}^{v_5}(q_g^{v_5})$ and merge into a single node. Then the geometry motion planning is used to plan the motions of v_5' and v_5'' and control them to the target positions for merging. Finally, merge them back to an individual node and then move the node to $q_g^{v_5}$. The detailed process is shown in Figure 26. The minimum length (L_{\min}) and the maximum length (L_{\max}) of all moving edge modules, the minimum angle between every pair of edge modules (θ_{\min}), and the motion manipulability (μ) are shown in Figure 27.

This motion task has been solved in Liu and Yim (2019) with the graph search algorithm exploring 8146 VTT configurations with a more complex action model in order to find a valid sequence of motion actions. With the proposed framework, the free space of v_5 is partitioned into

53 enclosed subspaces and it takes on average only 43.090 s to solve this motion task with a standard deviation of 4.424 s in 1000 trails, including the enclosed subspace computation, topology reconfiguration planning and two-node geometry reconfiguration planning, and the success rate is 100%.

8.2.2 Scenario 2 Another motion task in which topology reconfiguration actions are involved is shown in Figure 28 that is to move v_0 from a position $q_i^{v_0}$ inside the cubic truss (Figure 28a) to a new position $q_g^{v_0}$ (Figure 28b). The initial positions of all nodes are

$$\begin{aligned} q^{v_0} &= [0, 0, 1.075]^\top & q^{v_1} &= [1, 1, 0.075]^\top \\ q^{v_2} &= [-1, 1, 2.075]^\top & q^{v_3} &= [-1, -1, 2.075]^\top \\ q^{v_4} &= [1, -1, 2.075]^\top & q^{v_5} &= [1, 1, 0.075]^\top \\ q^{v_6} &= [-1, 1, 0.075]^\top & q^{v_7} &= [-1, -1, 0.075]^\top \\ q^{v_8} &= [1, -1, 0.075]^\top \end{aligned}$$

The constraints for this task are $\bar{L}_{\min} = 0.5$ m, $\bar{L}_{\max} = 5.0$ m, $\bar{\theta}_{\min} = 10^\circ$, and $\bar{\mu}_{\min} = 0.1$.

In this task, $q_g^{v_0} = [-0.64, -2.19, 2.78]^\top$. Similarly, $q_i^{v_0}$ and $q_g^{v_0}$ are in two separated enclosed subspaces, and one solution is to apply topology reconfiguration actions twice to traverse three enclosed subspaces in $\mathcal{C}_{\text{free}}^v$ shown in Figure 29. For this task, $d_{\min} = 0.5$, N_{\max} is constrained to be greater than or equal to 3, and $K = 8N_{\max}$.

The detailed planning result is shown in Figure 30. We first move the node v_0 to a location outside the cubic truss (Figure 30a — Figure 30c), and then split it into two. If

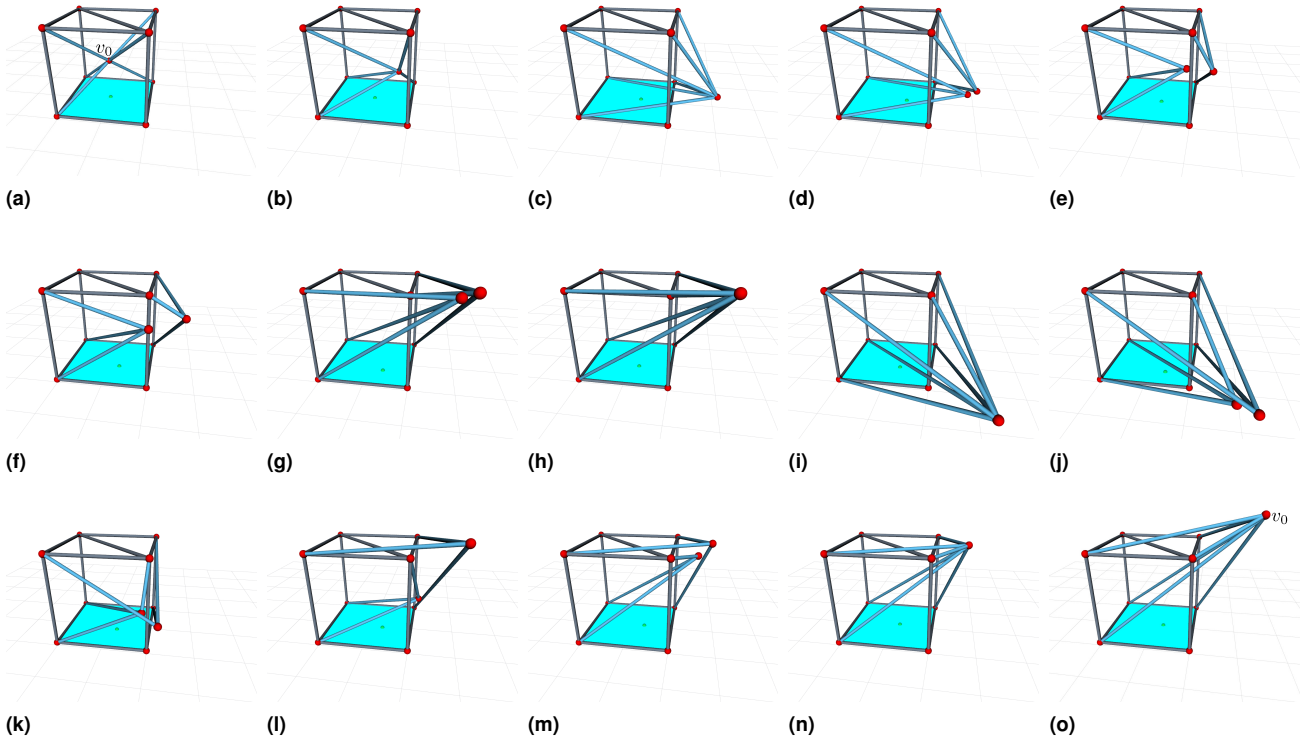


Figure 30. The sequence to move v_0 from $q_i^{v_0}$ to $q_g^{v_0}$ by traversing three enclosed subspaces in $\mathcal{C}_{\text{free}}^v$ is shown. (a) — (c) Move node v_0 to traverse the plane formed by node v_3, v_4, v_7 , and v_8 . (d) Split the node into a pair here so that both newly generated nodes can move around edge module (v_3, v_7) while avoiding singular configuration. (e) — (h) Two newly generated nodes are moved to a location inside the green enclosed subspace and merge. (i) — (j) Move the merged node to a new location and split it in a different way to generate two new nodes. (k) — (n) One node traverses the space inside the cubic truss to go to the blue enclosed subspace, and the other node moves upwards. Then these two nodes merge at a location inside the blue enclosed subspace. (o) Move the node to the target location to finish the task.

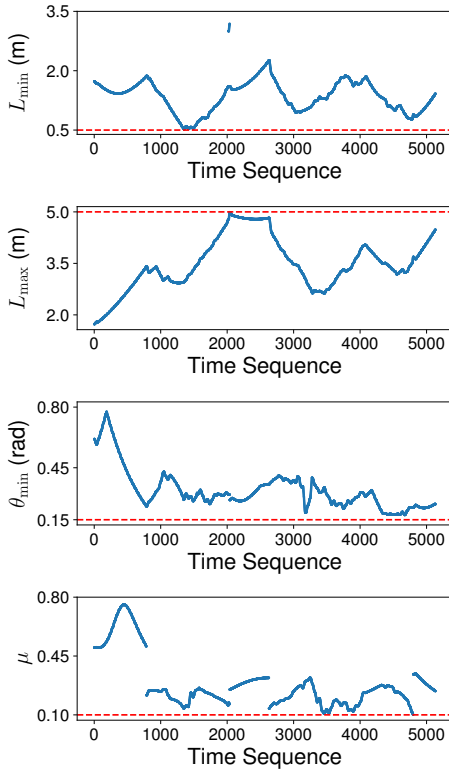


Figure 31. The minimum length (L_{\min}) and the maximum length (L_{\max}) of all moving edge modules, the minimum angle between every pair of edge modules (θ_{\min}), and the motion manipulability (μ) are measured throughout the topology reconfiguration process in Figure 30.

the node is split inside the cubic truss, there is no way to merge them inside the green enclosed subspace (Figure 30g) because one node has to traverse a region formed by node v_3 , v_4 , v_7 , and v_8 resulting in singular configurations. After this `Split` action, do geometry reconfiguration planning to control them to the green enclosed subspace and merge them back. Then move the node to a different location inside the green enclosed subspace (Figure 30i) and then split the node in a different way (Figure 30j) in order to navigate these two nodes to $C_{\text{free}}^v(q_g^{v_0})$ (Figure 30k — Figure 30m) and merge them in Figure 30n. Eventually move the node to $q_g^{v_0}$ (Figure 30o). The minimum length (L_{\min}) and the maximum length (L_{\max}) of all moving edge modules, the minimum angle between every pair of edge modules (θ_{\min}), and the motion manipulability (μ) are shown in Figure 31. The average planning time is 316.599 s with a standard deviation being 18.258 s in 100 trials, and the success rate is 68%. In these tests, the maximum consuming time is 360.187 s and the minimum is 258.647 s. The search space is larger and more samples are generated in order to find the sequence of topology reconfiguration actions which consumes more time.

8.3 Locomotion

The VTT used for the locomotion test is shown in Figure 32a that is an octahedron with three additional edge modules

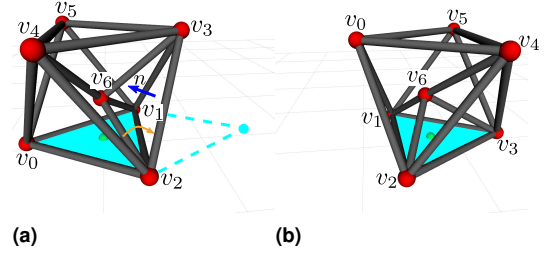


Figure 32. The locomotion task is to roll the truss from (a) to (b).

internally. The initial locations of all nodes are

$$\begin{aligned} q^{v_0} &= [-0.7217, 0, 0.075]^T \\ q^{v_1} &= [0.3608, 0.6250, 0.075]^T \\ q^{v_2} &= [0.3608, -0.6250, 0.075]^T \\ q^{v_3} &= [0.7217, 0, 1.0956]^T \\ q^{v_4} &= [0.7217, 0, 1.0956]^T \\ q^{v_5} &= [-0.3608, -0.6250, 1.0956]^T \\ q^{v_6} &= [0, 0, 0.5853]^T \end{aligned}$$

The constraints for this locomotion task are $\bar{L}_{\min} = 0.3$ m, $\bar{L}_{\max} = 5.0$ m, $\bar{\theta}_{\min} = 0.3$ rad, and $\bar{\mu}_{\min} = 0.1$. The task is to roll this VTT to an adjacent support polygon shown in Figure 32b, and the locomotion command is (v_1, v_2) . Five nodes (v_0 , v_3 , v_4 , v_5 , and v_6) are involved in this process and their goal locations can be computed by Eq. (17).

The detailed locomotion process is shown in Figure 33. Five nodes are divided into three groups and the whole process is also divided into three phases automatically. In the first phase, v_3 and v_5 are moved to expand the support polygon (Figure 33c). Then v_0 and v_4 are moved gradually to move the center of mass towards the adjacent support polygon shown in Figure 33d. Once the center of mass represented on the ground is inside the target support polygon, v_0 can be lifted off the ground and both v_0 and v_4 can be moved to their target locations (Figure 33e—Figure 33h). Finally, move node v_6 to its target location shown in Figure 33j to finish the whole process.

The minimum length (L_{\min}) and the maximum length (L_{\max}) of all moving edge modules, the minimum angle between every pair of edge modules (θ_{\min}), and the motion manipulability (μ) are shown in Figure 34. We randomly generate 1000 rolling commands and the average planning time is 8.297 s with the standard deviation being 5.935 s in 1000 trials, and the success rate is 100%. In these tests, the maximum consuming time is 24.459 and the minimum consuming time is 0.473 s. The locomotion of this VTT is also tested by Park et al. (2020) and the performance comparison is shown in Table 1. Our planner has better performance in terms of both efficiency and robustness.

An octahedron rolling gait is computed based on an optimization approach by Usevitch et al. (2020). Impacts

Table 1. Comparison with Park et al. (2020).

	Avg. Plan Time	Success Rate
Optimization	18.834 s	38.3% (820 trials)
Sampling-Based	8.297 s	100% (1000 trials)

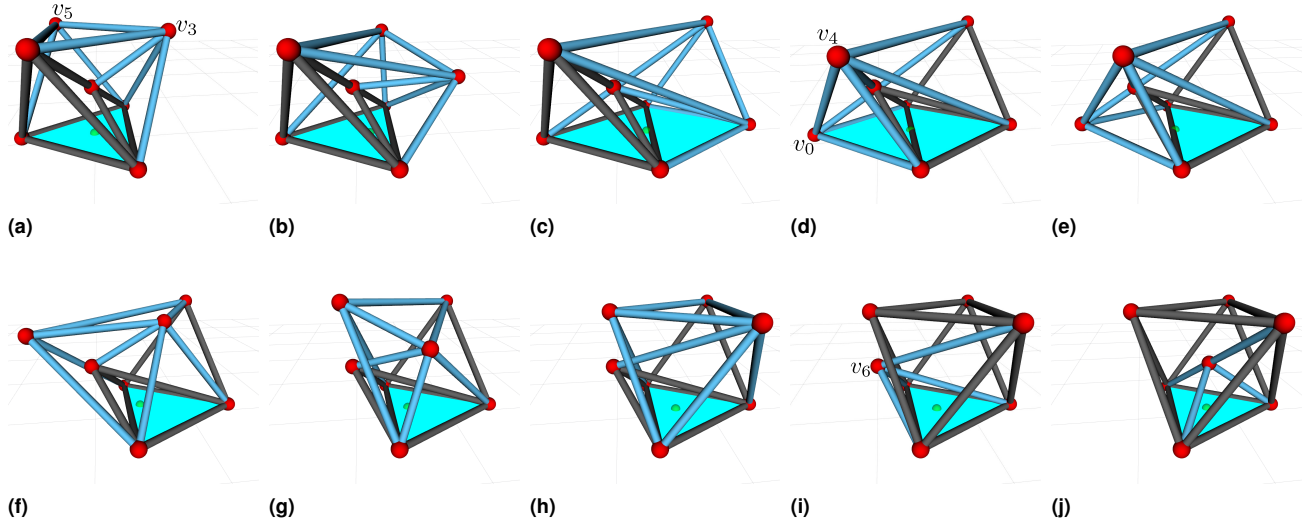


Figure 33. The planned motion for this locomotion task. (a) — (c) Move node v_3 and v_5 to first expand the support polygon. (d) Move v_0 and v_4 to move the center of mass towards the target support polygon. (e) — (h) Once the center of mass represented on the ground is inside the target support polygon, lift v_0 and move both v_0 and v_4 to their target locations. (i) — (j) Finally move v_6 to its target location to finish the locomotion process.

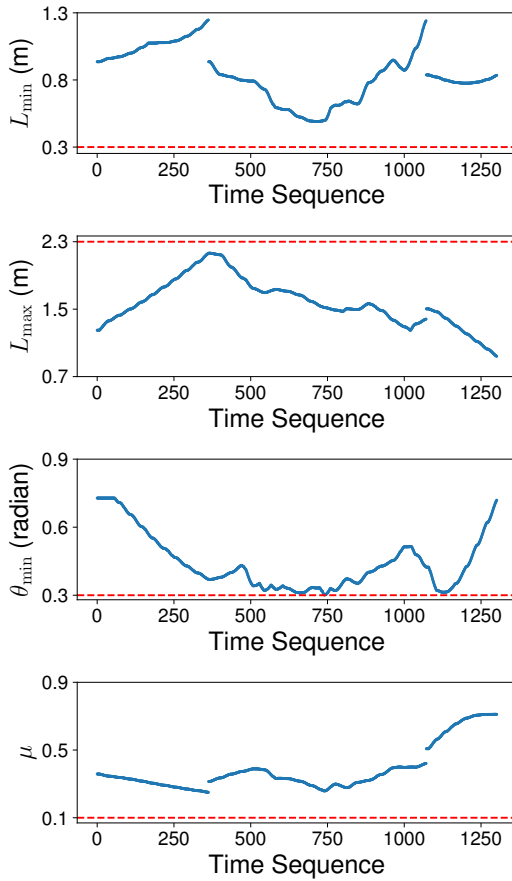


Figure 34. The minimum length (L_{\min}) and the maximum length (L_{\max}) of all moving edge modules, the minimum angle between every pair of edge modules (θ_{\min}), and the motion manipulability (μ) are measured throughout the locomotion process in Figure 33.

are not considered in this approach and it takes 166 s to compute the whole process. The octahedron configuration is also tested with our framework and the comparison is shown

Table 2. Comparison with [Usevitch et al. \(2020\)](#).

	Avg. Plan Time	Success Rate
Optimization	166 s	Not provided
Sampling-Based	1.181 s	100% (1000 trials)

in Table 2. The solution (Figure 19) can be derived as fast as 1.181 s in average with the standard deviation being 1.033 s in 1000 trials, and the success rate is 100%. In these tests, the maximum consuming time is 3.437 s and the minimum consuming time is 0.103 s.

9 Conclusion

A motion planning framework for variable topology truss robots is presented in this paper, including reconfiguration and locomotion. The configuration space of a node is studied considering the physical size of the robot components and singularity avoidance constraints. Geometry reconfiguration planning involves the motions of multiple nodes which are strongly coupled. An efficient algorithm to compute the obstacle regions and free space of a group is developed so that RRT can be applied to solve the geometry reconfiguration planning problem easily with all hardware constraints considered. A fast algorithm to compute all enclosed subspaces in the free space of a node is presented so that we can verify whether topology reconfiguration actions are needed. A sample generation method is introduced to generate samples that can efficiently provide valid topology reconfiguration actions over a wide space. With our topology reconfiguration planning algorithm based on Dijkstra's algorithm, a sequence of topology reconfiguration actions can then be computed with geometry reconfiguration planning for a group of nodes, and the motion tasks requiring topology reconfiguration can then be solved efficiently. A non-impact rolling locomotion algorithm is presented to move an arbitrary VTT easily by a simple command

with our efficient geometry reconfiguration planner. Our locomotion algorithm outperforms other approaches in terms of efficiency and robustness. These works can also be applied to other truss robots.

References

- Abrahantes M, Nelson L and Doorn P (2010) Modeling and gait design of a 6-tetrahedron walker robot. In: *2010 42nd Southeastern Symposium on System Theory (SSST)*. pp. 248–252. DOI:10.1109/SSST.2010.5442831.
- Agrawal SK, Kissner L and Yim M (2001) Joint solutions of many degrees-of-freedom systems using dextrous workspaces. In: *Proceedings 2001 ICRA. IEEE International Conference on Robotics and Automation (Cat. No.01CH37164)*, volume 3. pp. 2480–2485 vol.3. DOI:10.1109/ROBOT.2001.932995.
- Barber CB, Dobkin DP and Huhdanpaa H (1996) The quickhull algorithm for convex hulls. *ACM Trans. Math. Softw.* 22(4): 469–483. DOI:10.1145/235815.235821.
- Butler Z, Kotay K, Rus D and Tomita K (2004) Generic decentralized control for lattice-based self-reconfigurable robots. *The International Journal of Robotics Research* 23(9): 919–937. DOI:10.1177/0278364904044409.
- Casal A and Yim M (1999) Self-reconfiguration planning for a class of modular robots. In: McKee GT and Schenker PS (eds.) *Sensor Fusion and Decentralized Control in Robotic Systems II*, volume 3839. International Society for Optics and Photonics, SPIE, pp. 246 – 257. DOI:10.1117/12.360345.
- Collins F and Yim M (2016) Design of a spherical robot arm with the spiral zipper prismatic joint. In: *2016 IEEE International Conference on Robotics and Automation (ICRA)*. pp. 2137–2143. DOI:10.1109/ICRA.2016.7487363.
- Fromherz M, Hogg T, Shang Y and Jackson W (2001) Modular robot control and continuous constraint satisfaction. In: *Proceedings of IJCAI Workshop on Modelling and Solving Problems with Constraints*. Seattle, WA, pp. 47–56.
- Gilpin K, Kotay K, Rus D and Vasilescu I (2008) Miche: Modular shape formation by self-disassembly. *The International Journal of Robotics Research* 27(3-4): 345–372. DOI:10.1177/0278364907085557.
- Graham R (1972) An efficient algorithm for determining the convex hull of a finite planar set. *Information Processing Letters* 1(4): 132 – 133. DOI:https://doi.org/10.1016/0020-0190(72)90045-2.
- Hamlin GJ and Sanderson AC (1997) TETROBOT: A modular approach to parallel robotics. *IEEE Robotics Automation Magazine* 4(1): 42–50. DOI:10.1109/100.580984.
- Hou F and Shen WM (2014) Graph-based optimal reconfiguration planning for self-reconfigurable robots. *Robotics and Autonomous Systems* 62(7): 1047 – 1059. DOI:https://doi.org/10.1016/j.robot.2013.06.014.
- Jarvis R (1973) On the identification of the convex hull of a finite set of points in the plane. *Information Processing Letters* 2(1): 18 – 21. DOI:https://doi.org/10.1016/0020-0190(73)90020-3.
- Jeong S, Kim B, Park S, Park E, Spinos A, Carroll D, Tsabedze T, Weng Y, Seo T, Yim M, Park FC and Kim J (2018) Variable topology truss: Hardware overview, reconfiguration planning and locomotion. In: *2018 15th International Conference on Ubiquitous Robots (UR)*. pp. 610–615. DOI:10.1109/URAI.2018.8441880.
- Kettner L (1999) Using generic programming for designing a data structure for polyhedral surfaces. *Computational Geometry* 13(1): 65–90. DOI:https://doi.org/10.1016/S0925-7721(99)00007-3. URL <https://www.sciencedirect.com/science/article/pii/S0925772199000073>.
- Komendera E and Correll N (2015) Precise assembly of 3d truss structures using mle-based error prediction and correction. *The International Journal of Robotics Research* 34(13): 1622–1644. DOI:10.1177/0278364915596588.
- Liu C, Whitzer M and Yim M (2019a) A distributed reconfiguration planning algorithm for modular robots. *IEEE Robotics and Automation Letters* 4(4): 4231–4238. DOI:10.1109/LRA.2019.2930432.
- Liu C and Yim M (2019) Reconfiguration motion planning for variable topology truss. In: *2019 IEEE/RSJ International Conference on Intelligent Robots and Systems (IROS)*. pp. 1941–1948. DOI:10.1109/IROS40897.2019.8967640.
- Liu C and Yim M (2021) A quadratic programming approach to manipulation in real-time using modular robots. *The International Journal of Robotic Computing* 3(1): 121–145. DOI:10.35708/RC1870-126268.
- Liu C, Yu S and Yim M (2019b) Shape morphing for variable topology truss. In: *2019 16th International Conference on Ubiquitous Robots (UR)*. Jeju, Korea.
- Liu C, Yu S and Yim M (2020) A fast configuration space algorithm for variable topology truss modular robots. In: *2020 IEEE International Conference on Robotics and Automation (ICRA)*. pp. 8260–8266. DOI:10.1109/ICRA40945.2020.9196880.
- Liu C, Yu S and Yim M (2020) Motion planning for variable topology truss modular robot. In: *Proceedings of Robotics: Science and Systems*. Corvallis, Oregon, USA. DOI:10.15607/RSS.2020.XVI.052.
- Lyder A, Garcia RFM and Stoy K (2008) Mechanical design of Odin, an extendable heterogeneous deformable modular robot. In: *2008 IEEE/RSJ International Conference on Intelligent Robots and Systems*. pp. 883–888. DOI:10.1109/IROS.2008.4650888.
- Miura K (1984) Design and operation of a deployable truss structure. In: *NASA. Goddard Space Flight Center The 18th Aerospace Mech. Symp.* Greenbelt, Maryland, pp. 49–63. DOI: 19840017014.
- Murata S, Yoshida E, Kamimura A, Kurokawa H, Tomita K and Kokaji S (2002) M-TRAN: Self-reconfigurable modular robotic system. *IEEE/ASME Transactions on Mechatronics* 7(4): 431–441. DOI:10.1109/TMECH.2002.806220.
- Park S, Bae J, Lee S, Yim M, Kim J and Seo T (2020) Polygon-based random tree search planning for variable geometry truss robot. *IEEE Robotics and Automation Letters* 5(2): 813–819. DOI:10.1109/LRA.2020.2965871.
- Park S, Park E, Yim M, Kim J and Seo TW (2019) Optimization-based nonimpact rolling locomotion of a variable geometry truss. *IEEE Robotics and Automation Letters* 4(2): 747–752. DOI:10.1109/LRA.2019.2892596.
- Salemi B, Moll M and Shen W (2006) SUPERBOT: A deployable, multi-functional, and modular self-reconfigurable robotic system. In: *2006 IEEE/RSJ International Conference on Intelligent Robots and Systems*. pp. 3636–3641. DOI:10.1109/IROS.2006.281719.
- Spinos A, Carroll D, Kientz T and Yim M (2017) Variable topology truss: Design and analysis. In: *2017 IEEE/RSJ International*

- Conference on Intelligent Robots and Systems (IROS)*. pp. 2717–2722. DOI:10.1109/IROS.2017.8206098.
- Sucan IA, Moll M and Kavraki LE (2012) The open motion planning library. *IEEE Robotics Automation Magazine* 19(4): 72–82. DOI:10.1109/MRA.2012.2205651.
- Suh JW, Homans SB and Yim M (2002) Telecubes: Mechanical design of a module for self-reconfigurable robotics. In: *Proceedings 2002 IEEE International Conference on Robotics and Automation (Cat. No.02CH37292)*, volume 4. pp. 4095–4101 vol.4. DOI:10.1109/ROBOT.2002.1014385.
- Usevitch N, Hammond Z, Follmer S and Schwager M (2017) Linear actuator robots: Differential kinematics, controllability, and algorithms for locomotion and shape morphing. In: *2017 IEEE/RSJ International Conference on Intelligent Robots and Systems (IROS)*. pp. 5361–5367. DOI:10.1109/IROS.2017.8206431.
- Usevitch NS, Hammond ZM and Schwager M (2020) Locomotion of linear actuator robots through kinematic planning and nonlinear optimization. *IEEE Transactions on Robotics* : 1–18 DOI:10.1109/TRO.2020.2995067.
- Woo Ho Lee and Sanderson AC (2002) Dynamic rolling locomotion and control of modular robots. *IEEE Transactions on Robotics and Automation* 18(1): 32–41. DOI:10.1109/70.988972.
- Yim M, Duff DG and Roufas KD (2000) PolyBot: A modular reconfigurable robot. In: *Proceedings 2000 ICRA. Millennium Conference. IEEE International Conference on Robotics and Automation. Symposia Proceedings (Cat. No.00CH37065)*, volume 1. pp. 514–520 vol.1. DOI:10.1109/ROBOT.2000.844106.
- Yim M, Shen W, Salemi B, Rus D, Moll M, Lipson H, Klavins E and Chirikjian GS (2007) Modular self-reconfigurable robot systems [grand challenges of robotics]. *IEEE Robotics Automation Magazine* 14(1): 43–52. DOI:10.1109/MRA.2007.339623.
- Yim M, White P, Park M and Sastra J (2009) Modular self-reconfigurable robots. In: Meyers RA (ed.) *Encyclopedia of Complexity and Systems Science*. New York, NY: Springer New York. ISBN 978-0-387-30440-3, pp. 5618–5631. DOI: 10.1007/978-0-387-30440-3_334.